FERMILAB-THESIS-1999-61

学　位　論　文

半　田　隆　信

FERMILAB-THESIS-1999-61

Search for Technicolor Particles in $p\bar{p}$ Collisions at $\sqrt{s}$ = 1.8 TeV

（重心系エネルギー 1.8 TeV 陽子・反陽子衝突におけるテクニカラー粒子探索）

1999年2月

広島大学理学研究科物理学専攻

半田隆信

目次

主論文

Search for Technicolor Particles in $p\bar{p}$ Collisions at $\sqrt{s}$ = 1.8 TeV

（重心系エネルギー 1.8 TeV 陽子・反陽子衝突におけるテクニカラー粒子探索）

公表論文

（1）Search for Higgs Bosons Produced in Association with a Vector Boson in $p\bar{p}$ Collisions at $\sqrt{s}$ = 1.8 TeV

（重心系エネルギー 1.8 TeV 陽子・反陽子衝突におけるヒッグス粒子探索）

Physical Review Letters, Volume 81, Number 26, 5748-5753

（2）Measurement of the Top Quark Mass with the Collider Detector at Fermilab

（フェルミ研究所 CDF 実験におけるトップクォーク質量の測定）

Physical Review Letters, Volume 82, Number 2, 271-276

参考論文

（1） Micro-discharge noise and radiation damage of silicon microstrip sensors

（シリコンマイクロストリップ検出器の微小放電ノイズと放射線損傷）

Nuclear Instruments and Methods in Physics Research A 383 166-173

（2） Measurement of the $t\bar{t}$ Production Cross Setion
in $p\bar{p}$ Collisions at $\sqrt{s}$ = 1.8 TeV

（重心系エネルギー 1.8 TeV 陽子・反陽子衝突における
トップクォーク対生成断面積の測定）

Physical Review Letters, Volume 80, Number 13, 2773-2778

（3） Observation of the B_c Meson in $p\bar{p}$ Collisions at $\sqrt{s}$ = 1.8 TeV

（重心系エネルギー 1.8 TeV 陽子・反陽子衝突における B_c 中間子の発見）

Physical Review Letters, Volume 81, Number 12, 2432-2437

（4） Search for Second Generation Leptoquarks in the
Dimuon Plus Dijet Channel of $p\bar{p}$ Collisions at $\sqrt{s}$ = 1.8 TeV

（重心系エネルギー 1.8 TeV 陽子・反陽子衝突における
第2世代レプトクォークの探索）

Physical Review Letters, Volume 81, Number 22, 4806-4811

主論文

FERMILAB-THESIS-1999-61

Search for Technicolor Particles in $p\bar{p}$ Collisions at $\sqrt{s} = 1.8$ TeV

Takanobu Handa

February 1999

Department of Physics, Faculty of Science
Hiroshima University

Abstract

We describe a search for technicolor particles at the CDF (Collider Detector at the Fermilab) experiment in $p\bar{p}$ collisions at $\sqrt{s}$=1.8 TeV . We search for color singlet technirho and technipion by analyzing the final state consisting of leptonically decayed W boson and two jets requiring at least one b quark tagging.

As one of models which are beyond the present standard model of elementary particles, a recent technicolor model expects a color singlet technirho production in high energy $p\bar{p}$ collisions. In the CDF experiment, the W boson and the technipion decay mode of the technirho has the largest branching ratio when the masses of the technipion and the technirho are around 90 GeV/c^2 and 180 GeV/c^2 , respectively. In this mass combination region, the production cross section times branching ratio of the decay mode is estimated to be sufficiently large for searching the technipion and the technirho in the CDF data of an integrated luminosity of $109 \pm 7\,\mathrm{pb}^{-1}$. The neutral technipion would decay mostly to a pair of b quarks, and the charged technipion would decay mostly to a b quark and a c quark. The leptonic ($e\nu$ or $\mu\nu$) decay mode of the W boson gives us much cleaner signal compared to the dijet decay mode of the W boson. In this analysis accordingly, we concentrate ourselves on these two modes : $\rho_T^{\pm} \to W\pi_T^0 \to l\nu b\bar{b}$ and $\rho_T^0 \to W\pi_T^{\pm} \to l\nu b\bar{c}$. Here, the l represents electron or muon. We search for a technipion mass resonance in the invariant mass distribution of the b-tagged two jets system and a technirho mass resonance in the invariant mass distribution of the W and b-tagged two jets system.

Any signature of the present model has not been found at all; the CDF data under consideration is completely consistent with the predictions of the Standard Model. From the statistics of the data and the background, we set an upper limit of the production cross section for each mass combination of the technipion and the technirho with 95 % confidence level and set an excluded region in the mass plane of these technicolor particles.

Acknowledgments

First I express my sincere gratitude to Professor Yoshio Sumi for his continuous guidance and encouragement. My special thanks are given to my advisor Professor Takashi Ohsugi for the advise and encouragement he has provided throughout my graduate course. I also acknowledge the support of Dr. Yohsei Iwata and Dr. Shoichi Yoshida.

Many people helped me greatly in my analysis in the Fermilab. In particular, without the daily discussion and help of Dr. Kaori Maeshima, I would never have finished my analysis. I thank her, Dr. Juan Valls, and Ms. Rocio Vilar as my colleagues of this analysis. By working with them, my two years stay in the Fermilab became very exciting and fulfilling. I would like to thank the members of the exotic physics group of CDF. I thank exotic group conveners Professor Henry Frisch, Dr. David Stuart, and Dr. John Conway. They suggested me many advises. Dr. David Toback gave me many pieces of information of the technicolor search when I started my analysis. Mr. Toshiharu Uchida, Dr. Mark Kruse, Dr. Robert Roser helped me finding proper CDF data set for this analysis. Dr. Thomas Baumann and Dr. Jorge Troconiz kindly helped me about a Pythia Monte Carlo code. Mr. Alexis Amadon and Dr. Weiming Yao gave me important information about W and two jets event selection. Dr. Guillaume Unal, Dr. Fotios Ptohos, Dr. Kara Hoffman, Mr. Toshiaki Kikuchi, and Dr. Takashi Asakawa helped me a lot about background study. The advice of Dr. Junichi Suzuki was important for my detector simulation study. I acknowledge Mr. Jeff Berryhill and Dr. Simona Rolli who helped me implementing a new Pythia Monte Carlo code to the CDF offline analysis. Dr. Takeshi Takano and Mr. Hosai Nakada kindly answered me for my many questions about PAW and CERNLIB analysis utilities.

I acknowledge Professor Kenneth Lane, Professor Estia Eichten, Dr. John Womersley and Professor Torbjorn Sjostrand for giving me a response of my questions about technicolor theory. Their new Pythia Monte Carlo code with a walking technicolor model is indispensable to this analysis.

I would like to thank Dr. Jeff Spalding as my supervisor in the Fermilab. He gave me a lot of experience of the research and development of silicon microstrip detectors. I thank many people in the SVX-II silicon microstrip detector group at CDF.

I thank to Professor Koji Takikawa who gave much effort for my international student exchange program. Professor Kunitaka Kondo and Professor Shinhong Kim gave me kind encouragement and advice. I also acknowledge Dr. Yoshihiro Seiya, Dr. Fumihiko Ukegawa, Dr. Teruki Kamon, Dr. Ryuichi Takashima and Dr. Itsuo Nakano for their advice. Mr. Hirotoshi Toyoda, Mr. Hirofumi Ikeda, Mr. Hiroyuki Minato, Dr. Tomoko Kuwabara, Mr. Koji Terashi, and Mr. Kenichi Hatakeyama are unforgettable friends as CDF Japanese students. I thank Ms. Kyoko Kunori who helped me a lot of office work and suggested me many things about American life.

I thank to many students in Hiroshima University. At first, I especially thank Mr. Takafumi Ohmoto who taught me a lot about CDF offline analysis and helped my first foreign life when I came to the Fermilab. I also thank to Mr. Koichi Kurino, Dr. Hiroaki Ohnishi, Mr. Kazuki Fujita, Mr. Hiroaki Kitabayashi, Mr. Yoshiyuki Takata, Mr. Takeshi Kohama, Mr. Kenichi Sato, Mr. Masahiro Ikeda, and Mr. Katsuma Ikematsu. I cannot also forget Mr. Kazuhiro Kaimi, who passed away at CERN during my stay in the Fermilab. A lot of discussions about physics with him was valuable for me. I pray that his soul is resting in peace.

Finally, I express my special gratitude for my family. My parents have kept giving me continuous support and encouragement since my born for twenty seven years. My brother Dr. Shinji Handa has been every time an aim of my life.

Contents

List of Figures

List of Tables

Chapter 1

Introduction

1.1 Technicolor Theory

The Standard Model of elementary particles explains existing experimental results extremely well. However, the mechanism of electroweak symmetry breaking is still experimentally uncovered. In the framework of the Standard Model, the electroweak symmetry is spontaneously broken by introducing fundamental scalar particles in the theory. These are eventually identified as W_L and Z_L and one or more Higgs bosons. Technicolor model appears as an alternative theory where the electroweak symmetry is dynamically broken [1, 2]. A new strong gauge (technicolor) force acts between new fermions (technifermions) to form bound states (technimesons) which become the observable W_L, Z_L and technipions [3].

Technicolor (TC), as originally conceived is not able to provide existing fermion masses. Also, some predicted technimesons are so light that they should have been discovered in e^+e^- annihilation experiments. Extended technicolor (ETC) theories solve these problems at the cost of introducing large flavor-changing neutral-currents (FCNC). Again, additional mechanisms must be added to the ETC theories to avert the FCNC problem. One solution put forward is walking technicolor (WTC), which generates fermion masses while suppressing FCNC interactions down to a comfortable level (see Ref. [4] for WTC signatures at Tevatron). Even still, ETC and WTC

cannot accommodate the large mass of the top quark. Topcolor assisted technicolo has recently been proposed as the mechanism responsible for generating the large to quark mass, in conjunction with TC and ETC providing the gauge boson masses an remaining quark masses [5].

The above discussion shows the evolution of the technicolor models from the ori inal formulation for dynamical electroweak symmetry breaking. Each iteration of th model-building addressed a shortcoming of the previous model.

In this paper, we report results of an experimental search for multiscale mode of walking technicolor including the topcolor-assisted technicolor scenario. We sear for the lightest pseudo-scalar mesons, technipions ($\pi_T^{\pm,0}$), and the lightest iso-tripl vector mesons, technirhos ($\rho_T^{\pm,0}$). Light scale technimesons generally consist of col singlets [5, 6] and non-singlets [4]. Here we consider color singlet technipions produc through the decay of color singlet technirhos.

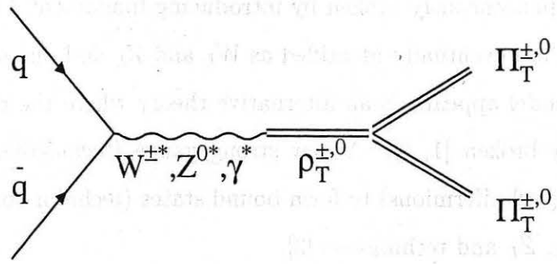

Figure 1.1: Technicolor isotriplet technipion pair production through the techni resonance.

In $p\bar{p}$ collider, the technirhos are produced in s-channel weak boson resonan as shown in Figure 1. The technirhos decay into a pair of the technicolor eigenst (massless Goldstone) technipions, $\Pi_T^{\pm,0}$. The technipions are the mixture of longitu nal component of weak bosons, $W_L^{\pm}$ and Z_L^0, and mass eigenstate (pseudo-Goldsto

technipions, $\pi_T^{\pm 0}$. In the simplest parameterization, it can be expressed as:

$$\begin{aligned} |\,\Pi_T^{\pm}> &= \sin\chi\,|\,W_L^{\pm}> \;+\; \cos\chi\,|\,\pi_T^{\pm}> \\ |\,\Pi_T^{0}> &= \sin\chi\,|\;Z_L^{0}> \;+\; \cos\chi\,|\,\pi_T^{0}> \end{aligned} \tag{1.1}$$

where $\sin\chi = F_T/F_\pi$. The F_π is the decay constant of technipions in the minimal technicolor model, that is defined as follows : [6]

$$F_\pi \equiv 2^{-\frac{1}{4}} G_F^{-\frac{1}{2}} = 246\,\mathrm{GeV}\ . \tag{1.2}$$

The F_T is the decay constant of technipions in the walking technicolor model, that is defined as:

$$F_T = \frac{F_\pi}{\sqrt{N_D}}\ , \tag{1.3}$$

where N_D is the number of technifermion doublets. In what follows, we assume the number of technifermion doublets is 9 and the value of mixing parameter ($\sin\chi$) is 1/3 [5].

All final states of diboson decay mode of the technirhos can be summarized as:

$$\begin{aligned} &\rho_T^{\pm} \to W^{\pm}Z^0,\ W^{\pm}\pi_T^0,\ \pi_T^{\pm}Z^0,\ \pi_T^{\pm}\pi_T^0\ , \\ &\rho_T^{0} \to W^{+}W^{-},\ W^{\pm}\pi_T^{\mp},\ \pi_T^{+}\pi_T^{-}\ . \end{aligned} \tag{1.4}$$

Among these final states, we search for $\rho_T^{\pm} \to W^{\pm}\pi_T^0$ and $\rho_T^0 \to W^{\pm}\pi_T^{\mp}$ decay modes as shown in Figure 1.2. These two modes have the two largest branching ratios in the mass region $M_W + M_{\pi_T} \le M_{\rho_T} \le 2M_{\pi_T}$. The production cross section times branching ratio is approximately 12 pb ($\rho_T^{\pm} \to W^{\pm}\pi_T^0$) and 5 pb ($\rho_T^0 \to W^{\pm}\pi_T^{\mp}$) at the masses of the technipion and the technirho being 90 GeV/c^2 and 180 GeV/c^2 , respectively [8].

The coupling strength of the technipion to fermions depends on the fermion masses and it is greater for the larger fermion mass. Hence, the technipion would mostly decay into $b\bar{b}$ or $b\bar{c}$ final state. For finding these final states, we can use the b-quark tagging technique (see Chapter 3.4) to significantly reduce the QCD W+ 2 jet background.

In this paper, we describe a search for the neutral and charged technipion production associated with a W boson through the technirho resonances. We will try to find leptonically (e or μ) decayed W's. The final states are as follows.

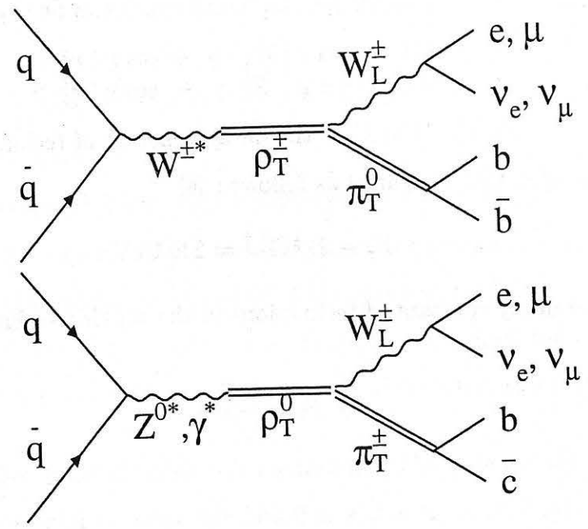

Figure 1.2: Leptonically decaying W plus technipion production through the technir resonances: $W + \pi_T^0$ and $W + \pi_T^{\pm}$.

$$\rho_T^{\pm} \to W\pi_T^0 \to e\nu b\bar{b}, \mu\nu b\bar{b}$$
$$\rho_T^0 \to W\pi_T^{\pm} \to e\nu b\bar{c}, \mu\nu b\bar{c} \quad (1$$

1.2 Production Cross Section

In $p\bar{p}$ collisions, the calculation of the production cross section is not easy because t initial parton momenta cannot be known uniquely. We obtain technicolor partic production cross section in $p\bar{p}$ collisions using the PYTHIA version 6.1 Monte Ca generator [9]. The PYTHIA carries out many calculation trials to the leading orc integrates over initial parton momenta, and calculate the mean value of the cr section. In each trial, the initial parton momenta are generated according to a par distribution function (p.d.f.) in a proton or antiproton. We use the MRSG [12] pro parton distribution function. To obtain the actual production cross section incluc higher order effect, we multiply a K-factor to the PYTHIA output. The value is deri

process		p.d.f.	σ	σ * 1.5	σ* 1.3
Z^0 (ee)	PYTHIA	EHLQ1	152 pb	228 pb	
Z^0 (ee)	PYTHIA	MRSG	176 pb		229 pb
Z^0 (ee)	PYTHIA	CTEQ4L	177 pb		230 pb
TC	PYTHIA	EHLQ1	11.2 pb	16.8 pb	
TC	PYTHIA	MRSG	13.4 pb		17.5 pb
TC	PYTHIA	CTEQ4L	13.3 pb		17.3 pb
TC	th. calc.	EHLQ1		18.1 pb	

Table 1.1: Comparison of cross section times branching ratio using different p.d.f. and K-factor values for Z^0 boson and technicolor particle productions. Here, mass of technipion is 90 GeV/c^2 and technirho is 180 GeV/c^2 .

using the following formula [13]:

$$K = 1 + \frac{\alpha_s}{2\pi}\frac{4}{3}\left(1 + \frac{4}{3}\pi^2\right) \quad (1.6)$$

Here, the α_s represents the strong force coupling constant. The α_s varies as a function of Q^2, but the Q^2 dependence is small in our search region. The value of α_s is assumed to be around 0.1 in the Q^2 range between 160 GeV/c^2 and 240 GeV/c^2 , which corresponds to the technirho mass region in our search. A K-factor value of 1.3 is obtained with the α_s value (K-factor values for the mass scale of 90, 160, and 240 GeV/c^2 are 1.33, 1.31, and 1.29, respectively.)

We checked technicolor production cross section values by comparing the PYTHIA output with a theoretical calculation [1]. The theoretical value uses leading order calculation with EHLQ1 parton distribution function and K-factor of 1.5 which is appropriate for EHLQ1 p.d.f. [8]. We used the same p.d.f. (EHLQ1) in PYTHIA and the same K-factor value (= 1.5) for the comparison. We found that the PYTHIA and the theoretical calculations agree fairly well (within 5 - 10 %). These values are shown in table 1.1.

[1] by Ken Lane

We then investigated the variation of the cross sections when we use various p.d.f We examined Z^0 boson production cross section as well as technicolor productio cross section using EHLQ1, MRSG, and CTEQ4L. The result is summarized in Table 1.1 Use of K-factor of 1.5 for EHLQ1 , K-factor of 1.3 for CTEQ4L, and MRSG, PYTHI gives consistent values in each other, and Z^0 cross section is consistent with wha we measure at the CDF [10]. Therefore we decide to use one of the recent leadin order p.d.f., MRSG and a K-factor value, 1.3, as described above for our technicol production cross section calculation.

Figure 1.3 shows the production cross section of the $p\bar{p}$ collision at $\sqrt{s} = 1$ TeV for all the diboson decay modes. In the plot, the technipion mass is assume to be 90 GeV/c^2 . At this technipion mass, the $W+\pi_T^0$ decay mode has the large cross section, about 12 pb at M(ρ_T)=180 GeV/c^2 . Figure 1.4 shows a similar plot wi the technipion mass of 70 GeV/c^2 . At this technipion mass, the multijet sample wi double b-tag may be a good signature for technicolor particle search since technipi pair production decay mode has higher yield. We have done a search for technicol particles using multijet final state. The result is shown in reference [11].

Figure 1.5 and 1.6 present cross section contour plots in a plane of M(π_T) vs. M(ρ for $W + \pi_T^0$ and $W + \pi_T^{\pm}$ decay modes, respectively. The contour plot in Figure shows a sum of the $W+\pi_T^0$ and the $W+\pi_T^{\pm}$ cross sections. The maximum cross secti is estimated to be 17.5 pb for the technipion mass at 90 GeV/c^2 and the technirho m at 180 GeV/c^2 .

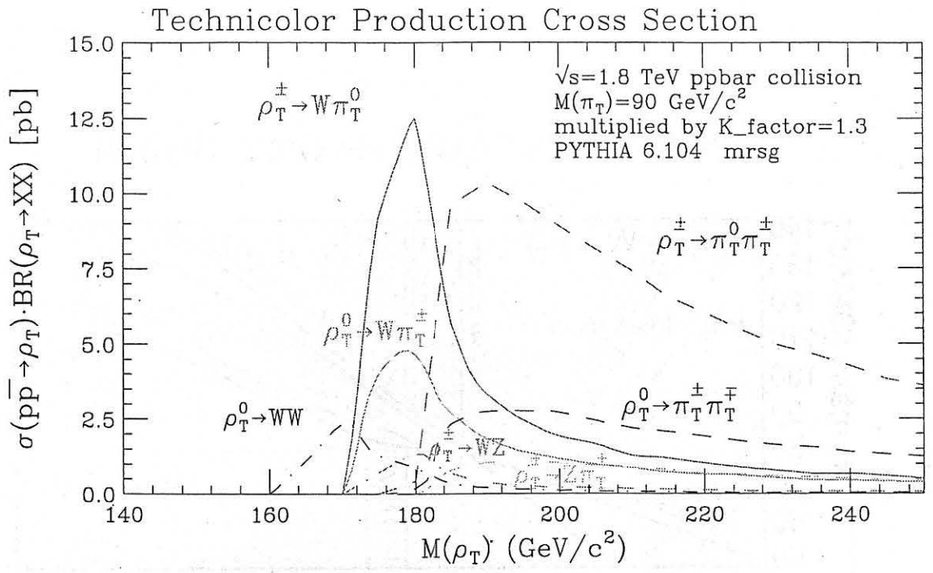

Figure 1.3: Production cross section times branching ratio for ρ_T as a function of ρ_T mass at $\sqrt{s}$=1.8 TeV $p\bar{p}$ collisions. The π_T mass is fixed to 90 GeV/c^2 . All diboson decay modes are shown. PYTHIA v 6.1 and MRSG pdflib are used. K-factor = 1.3 .

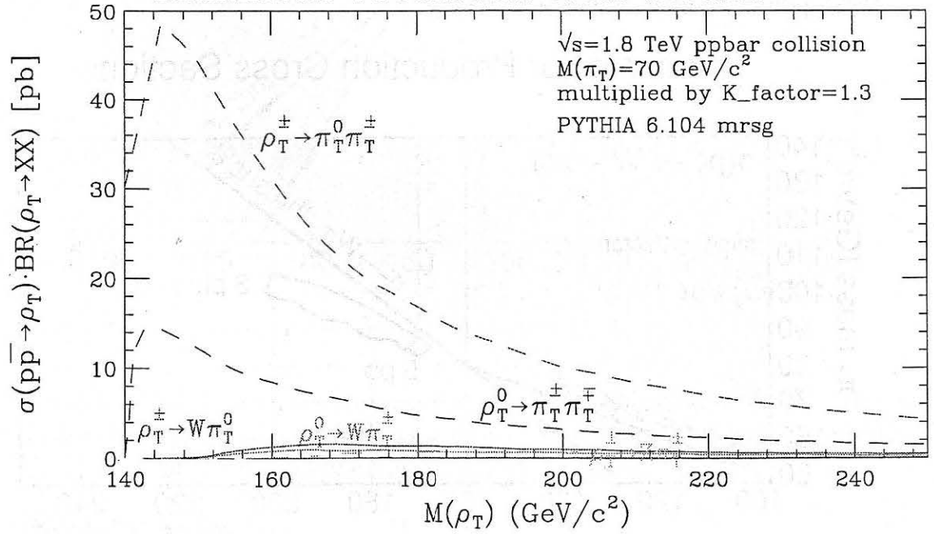

Figure 1.4: Production cross section times branching ratio for ρ_T as a function of ρ_T mass at $\sqrt{s}$=1.8 TeV $p\bar{p}$ collisions. The π_T mass is fixed to 70 GeV/c^2 . All the major diboson decay modes are shown. PYTHIA v 6.1 and MRSG pdflib are used. K-factor = 1.3 .

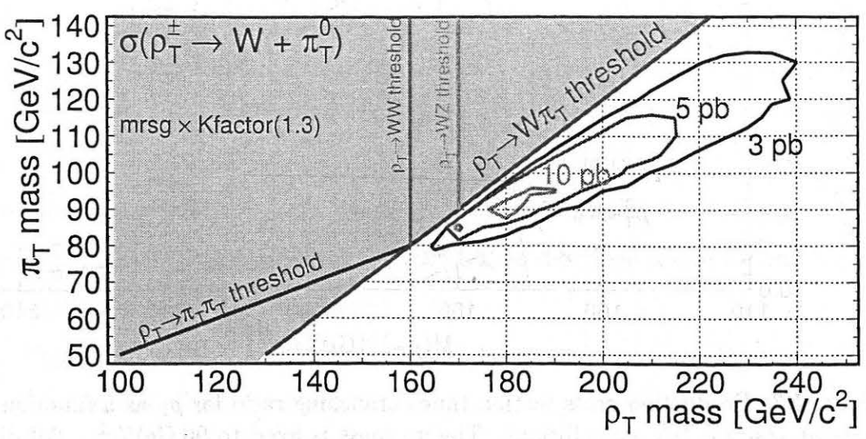

Figure 1.5: Production cross section times branching ratio of $\rho_T^{\pm} \to W+\pi_T^0$ $\sqrt{s}$=1.8 TeV $p\bar{p}$ collisions as a function of m(π_T) and m(ρ_T). PYTHIA v 6.1 a MRSG pdflib are used. K-factor = 1.3 .

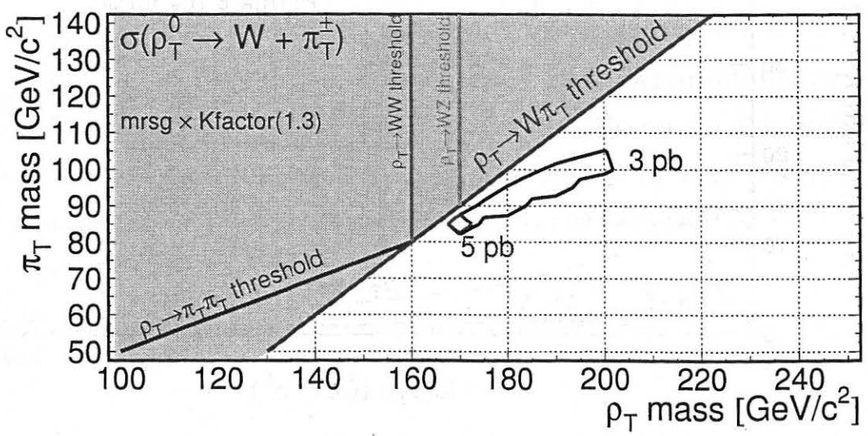

Figure 1.6: Production cross section times branching ratio of $\rho_T^0 \to W+\pi_T^{\pm}$ $\sqrt{s}$=1.8 TeV $p\bar{p}$ collisions as a function of m(π_T) and m(ρ_T). PYTHIA v 6.1 MRSG pdflib are used. K-factor = 1.3 .

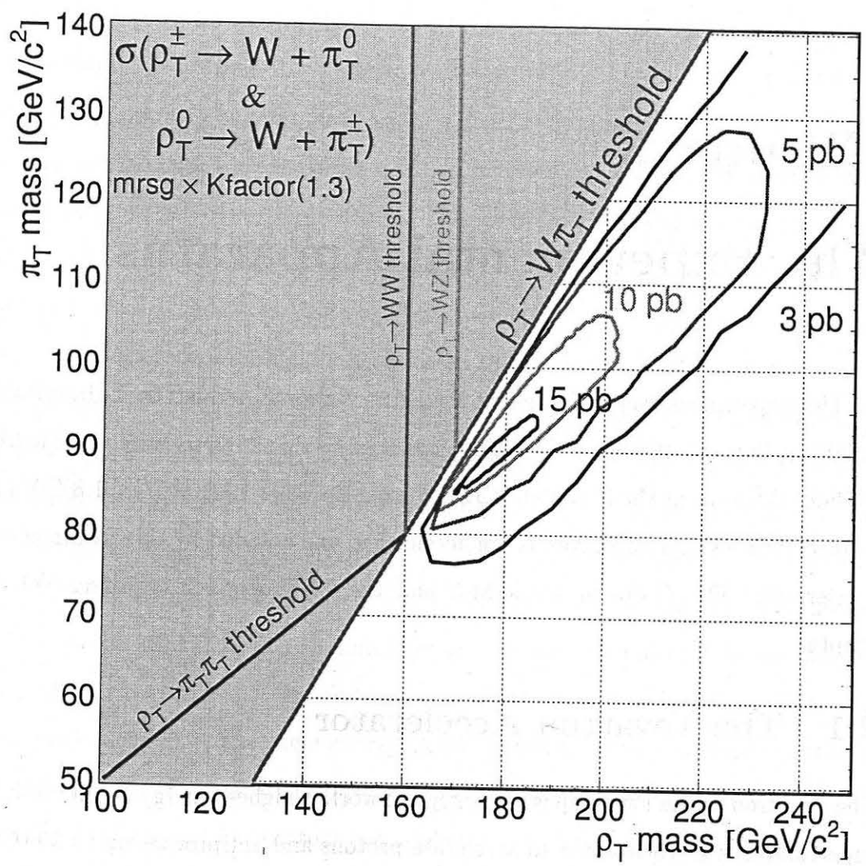

Figure 1.7: Production cross section times branching ratio of $\rho_T^{\pm} \to W+ \pi_T^0$ and $\rho_T^0 \to W+ \pi_T^{\pm}$ at $\sqrt{s}$=1.8 TeV $p\bar{p}$ collisions as a function of m(π_T) and m(ρ_T). PYTHIA v 6.1 and MRSG pdflib are used. K-factor = 1.3 .

Chapter 2

The Experimental Apparatus

This experiment was performed at the Fermi National Accelerator Laboratory (Fe milab) in Batavia, Illinois, U.S.A. The data used in this analysis were recorded by tl Collider Detector at the Fermilab (CDF) during the 1992-1995 at $\sqrt{s}$ =1.8 TeV $p\bar{p}$ cc lisions. Protons and anti-protons are accelerated and collided by the Tevatron collid accelerator. The Tevatron accelerator and the CDF detector are described in tl chapter.

2.1 The Tevatron Accelerator

The Tevatron at the Fermilab is currently the world's highest energy accelerator. It i superconducting synchrotron to accelerate protons and antiprotons up to 900 GeV high energy physics experiments. The circumference of the accelerator ring is kilometers in order to bend high energy proton beams. When it works in colli mode, the Tevatron provides proton-antiproton collisions at center of mass ene: $\sqrt{s} = 1.8$ TeV .

The Tevatron $p\bar{p}$ collider consists of five stage accelerators as illustrated in F ure 2.1. In the first stage, negatively charged hydrogen ions are accelerated to 750 k by a large DC voltage accelerator (Cockroft-Walton electrostatic accelerator). In Linac, a 150-meter-long linear accelerator, these particles are accelerated to 400 Me

The ions emerge from the LINAC through a carbon foil which strips their electrons to leave a bare proton beam. The booster ring, a synchrotron accelerator is 470 meters in circumference, where the protons from the LINAC are accelerated to 8 GeV . In the booster proton bunches are collected and injected into the Main ring. The Main ring, a synchrotron with a diameter of 2 kilometers, is composed of water-cooled magnets operated at room temperature. The protons are accelerated by the Main ring to 150 GeV and injected into the Tevatron ring. The Tevatron is a synchrotron with a diameter of 2 kilometers and consists of superconducting magnets cooled by liquid helium. The protons are finally accelerated to 900 GeV in the Tevatron.

Protons in the Main ring are also used to initiate production of antiprotons. The proton beam from the Main ring is directed to a tungsten target which produces antiprotons as a result. The typical production rate of the antiprotons is in order of 4×10^{10} $\bar{p}/hr$. The antiprotons are collected in the Debuncher ring and are reduced their spatial momentum dispersion by a process called stochastic cooling. The antiprotons are then transferred to the Accumulator ring, where the antiprotons are merged into a single beam cooled further, and stored. The Debuncher and Accumulator rings are operated at 8 GeV , the same energy as the Booster. After enough antiprotons have been accumulated, they are re-injected into the Main ring and accelerated to 150 GeV . Finally, protons and antiprotons are accelerated to 900 GeV by the Tevatron.

Proton and antiproton beams collide two places in the Tevatron ring, B0 and D0, housing Fermilab's two general purpose Collider detectors, CDF and D0 respectively. At the B0 interaction region where CDF exists, the beam is roughly Gaussian on its cross-section with a radius defined by one σ of $\sim$ 40μm. The beam is focused by quadrapole magnets which have the field strength of $\sim$ 5.7 Tesla. The longitudinal profile of the beam is approximately Gaussian with a length of 30 cm. The Tevatron has 6 bunches each of protons and antiprotons. The interaction interval is about 1.6 μs.

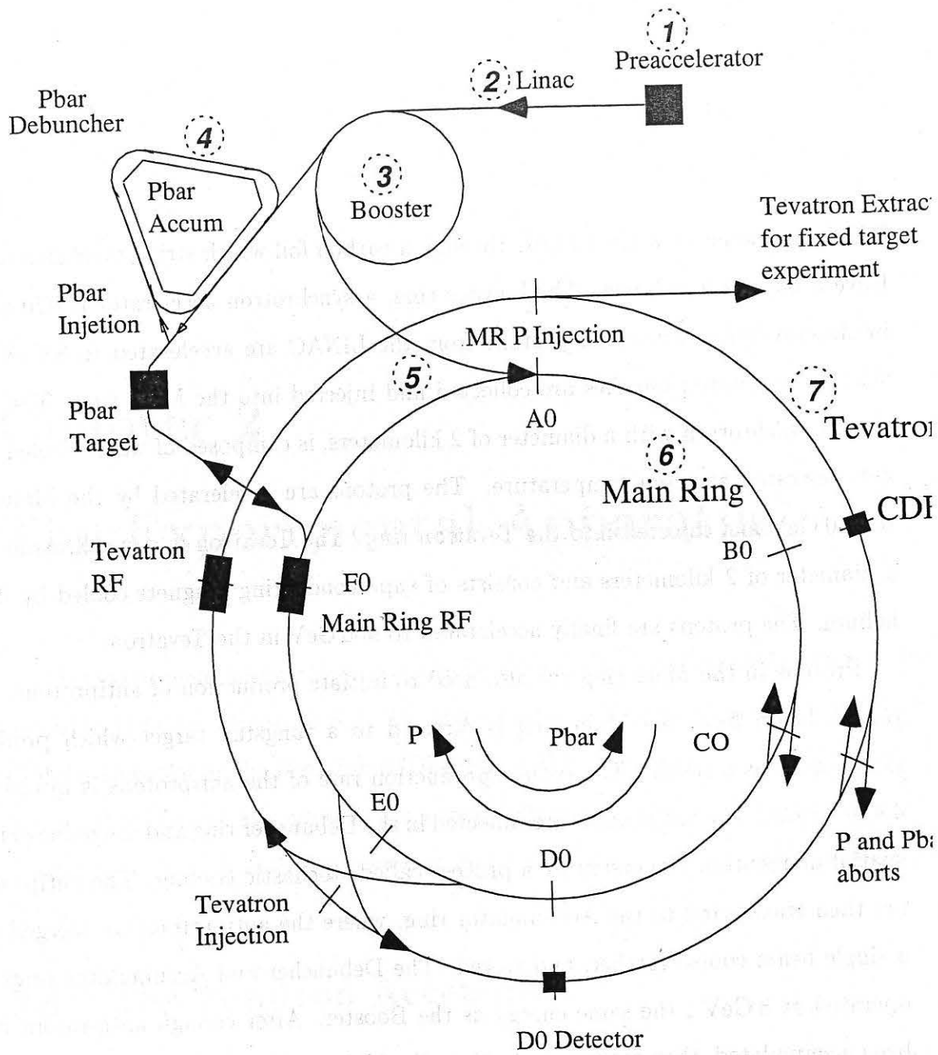

Figure 2.1: The Tevatron collider accelerator at the Fermilab.

The Tevatron provided an instantaneous luminosity of $\mathcal{L} \sim 1 \times 10^{31}$ cm^{-2}s^{-1} dur the period of 1992-1995 run. An integrated luminosity of 110 pb^{-1} has been collec by the CDF.

2.2 The CDF Detector

The collider Detector at Fermilab (CDF) is a general purpose detector designed to study the physics of high energy $p\bar{p}$ collisions. The CDF detector is described extensively many publications and is summarized in reference [17]. Here a brief overview of the CDF detector components related to the search for Technicolor particles is given.

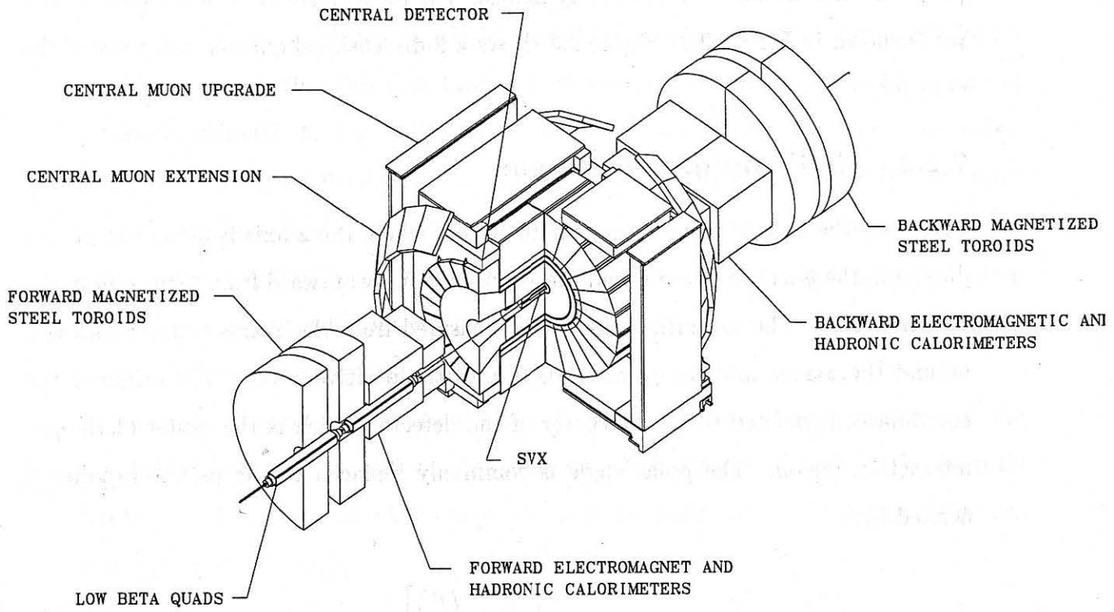

Figure 2.2: Perspective view of the Collider Detector at Fermilab.

2.2.1 Overview of the detector

The CDF is symmetrical in both azimuthal and forward-backward about the interac tion point located in the center of the CDF. A silicon vertex detector (SVX) is locate just outside of the beam pipe of the Tevatron. Tracking chambers (VTX,CTC) ar located inside a superconducting solenoidal magnet, and electro magnetic (EM) an hadronic (HAD) calorimeters directory outside of the magnet to measure the energ of electrons, photons, and hadron jets. The furthest components from the interactic points are muon chambers to identify muons. The perspective view of the CDF dete tor is shown in Figure 2.2. Figure 2.3 shows a 2-dimensional quarter side view of tl detector.

2.2.2 CDF coordinate system

CDF uses the a right handed coordinate system where the z-axis is along the prot direction, the y-axis is upward, and the x-axis is radially outward from the center of t Tevatron ring. The azimuthal angle ϕ is measured from the x-axis counterclockw around the z-axis, and the polar angle θ from the positive z-axis. The origin of t coordinates is defined to be the center of the detector which is the center of the i interaction region. The polar angle is commonly replaced to the pseudo-rapidity defined by:

$$\eta = -\ln\left[\tan\left(\frac{\theta}{2}\right)\right]. \qquad (2$$

It is invariant and additive under Lorenz transformation along the z-axis, and particle density per unit rapidity in $p\bar{p}$ collisions is approximately constant for $|\eta| <$ At high energy ($E \gg m$), the pseudorapidity is the good approximation of the rapic y defined by equation 2.2:

$$y = \frac{1}{2}\ln\left(\frac{E+p_z}{E-p_z}\right), \qquad (2.2)$$

where E is the energy and p_z is the z component of the momentum.

2.2.3 Tracking Detectors

Silicon Vertex Detector (SVX)

The SVX is designed to track particles near the interaction point and has the capability to distinguish sequential decay particles at the tens of microns level in the x-y plane.

The SVX consists of two identical barrels placed at both sides of z=0. Each barrel is 25.5 cm in length, with four layers of silicon detectors arranged in 12 sectors of ladders in azimuth Φ. Figure 2.4 shows the layout of the ladder for innermost layer. The innermost layer is located at r=3.0 cm from the beamline, and the outermost layer at r=7.8 cm from the beamline. Three sensors are mounted on each ladder structure, wire bonded together in pairs and read out at an end of the barrel. The axial strip pitch of each sensor is 60 μm except the outermost layer which has 55 μm strip pitch. Figure 2.5 shows an overall layout of one of its barrels.

Since $p\bar{p}$ interaction points are spread along the beam line direction with the standard deviation of $\sigma = 30$ cm, the geometrical acceptance of the SVX is about 60 % of $p\bar{p}$ collisions. The SVX covers the pseudorapidity of $\eta < 1.9$ if four hits are required in a SVX track.

Vertex Chamber (VTX)

The VTX is designed primarily to determine the event vertex position in the longitudinal z direction. The VTX provides tracking information up to a radius of 22 cm and $|\eta| < 3.25$. The VTX consists of eight octagonal modules mounted end-to-end along z axis and each module is segmented azimuthally into eight wedges. The wires are

perpendicular to the beam line and the radial centerline of the wedges. A resolutio of 1 mm along z axis of $p\bar{p}$ interaction vertices is achieved.

Central Tracking Chamber (CTC)

The CTC is a cylindrical drift chamber which has 1.3 m radius and 3.2 m length. I gives precise momentum measurements in the angular region $40° < \theta < 140°(-1 < \eta <$ 1). The chamber contains 84 layers of the sense wires grouped into 9 "super layers" Five of the super layers consist of 12 axial sense wires, while four stereo superlaye consist of six sense wires tilted by $\pm 3°$ relative to the beam direction. Figure 2.6 show the endplate of the chamber displaying 45° tilt superlayers to the radial direction t correct for the Lorenz angle of the electron drift in the magnetic field. The transvers momentum resolution of the CTC track alone is $\delta p_T/p_T^2 \leq 0.002(\text{GeV/c})^{-1}$. It improved to be $\delta p_T/p_T^2 \leq 0.001(\text{GeV/c})^{-1}$ when the beam position information additionally used in the track fit.

2.2.4 Calorimeters

The active sampling medium of the CDF calorimeters is either scintillator in the centr region ($|\eta| < 1.1$), or gas proportional chambers in the plug($1.1 < |\eta| < 2.4$) ar forward/backward ($2.4 < |\eta| < 4.2$) regions.

Central EM Calorimeter (CEM)

The CEM is a 31 layer lead scintillator sandwich type sampling calorimeter with wav length shifter to measure electron and photon energy. It consists of 24 wedges, ea covering 15° in ϕ and containing an electro magnetic (CEM) section followed by hadronic section (CHA). Each of the wedges made of ten projective towers, each co ering 0.1 units in $\Delta\eta$. The coverage region of the CEM is $|\eta| < 1.1$ and full in azimuth. The energy resolution is $13.7\%/\sqrt{E_T} \oplus 2\%$, where E_T is the transve

energy defined by

$$E_T \equiv E \sin\theta \tag{2.3}$$

with the observed energy (E) and polar angle (θ). Figure 2.7 shows the anatomy of an individual central calorimeter wedge.

Central electro-magnetic strip chamber (CES)

The central electro magnetic strip chambers (CES) are embedded at shower maximum position in the wedges of the CEM. The CES measures the position and transverse development of EM shower. The location of the CES is shown in Figure 2.3 and a schematic view of the CES is shown in Figure 2.8.

Central hadron calorimeter (CEM) and wall hadron calorimeter (WHA)

The CHA covers the full 2π azimuthal range and $|\eta| < 0.9$. The CHA is located outside of the CEM and it consists of 48 steel-scintillator modules each. To fill the gap between the CHA and PHA, the WHA covers the region $0.7 < |\eta| < 1.3$. Like the CHA, the WHA consists of 48 steel-scintillator modules each. The energy resolutions of the CHA and the WHA are $50\%/\sqrt{E} \oplus 3\%$ and $50\%/\sqrt{E} \oplus 3\%$, respectively.

Plug EM calorimeter (PEM)

The PEM is located 1.73 m in z from the nominal interaction point and covers $1.1 < |\eta| < 2.4$. It consists of 4 quadrants on each end, each quadrant consists of 34 layers of proportional tubes sandwiched between lead plates. The energy resolution of the PEM is $22\%/\sqrt{E} \oplus 2\%$. Near shower maximum position in the PEM, a layer with finer-spaced strips (PES) provides shower profile and precise position determination.

Plug hadron calorimeter (PHA)

The PEM is directly followed by the PHA. The PHA also employs gas proportion tubes. The radiator of the PHA is steel. The covering region of the PHA is $1.1 < |\eta|$ 2.4. The resolution is $106\%/\sqrt{E} \oplus 6\%$.

2.2.5 Muon detection

At CDF, muons are identified by a track in the CTC which is matched to a good quali track stub in one of the CDF muon detectors. These muon detectors are divided their pseudorapidity coverage. They are named the central drift chambers (CMU), t central muon upgrade (CMP), and the central muon extension chambers (CMX) shown in Figure 2.3

Central muon chambers (CMU and CMP)

The CMU and CMP muon detectors cover the pseudo rapidity region ($|\eta| < 0.$ Both detectors consist of four layers of single wire drift chambers which measure mu position in $r-\phi$ plane from drift time information. Approximately 84 % of the detec is covered by the CMU, 63 % by the CMP and 53 %.

The position resolution in $r - \phi$ plane view is $\sim 250\mu$m. The CMU additiona determines track z position by charge division. The CMU is placed between the cent hadronic calorimeter and the magnet return yoke. The amount of material before CMU and CMP is 5 and 8 interaction length, respectively.

Central Muon eXtension (CMX)

The muon coverage is extended by additional muon chambers in the pseudorapi range $0.6 < |\eta| < 1.0$. these are also constructed from single wire drift chamb There are scintillators on both sides of the CMX which are used for the CMX m

trigger. Figure 2.9 shows the $\eta - \phi$ muon coverage region for the CMU, CMP and CMX.

2.2.6 Beam-beam counters (BBCs)

The BBCs are composed of 16 scintillator plates plus several photomultipliers. They are positioned at 5.8 m from the nominal interaction point and they cover the pseudo-rapidity range $3.24 < |\eta| < 5.90$. Hits in both counters that coincide with the beam bunches crossing through the detector serve as both a minimum bias trigger and the primary luminosity monitor. The fragmented hadrons from the spectator quarks and gluons in the collided proton and anti-proton must leave signals in the high pseudo-rapidity region where BBCs exist. Signals are required in both BBCs within a 15 ns window about the collision time .

The instantaneous luminosity ($\mathcal{L}$) and integrated luminosity (L) can be obtained by following equations.

$$\mathcal{L} = \frac{R_{BBC}}{\sigma_{BBC}} \tag{2.4}$$

$$L = \frac{N_{BBC}}{\sigma_{BBC}} \tag{2.5}$$

The R_{BBC} is the rate of coincidences in BBCs, the N_{BBC} is number of coincidences in BBCs, and the σ_{BBC} is effective cross section of the BBCs. The BBC cross section as measured in reference [10] is 51.15±1.6 mb. Typical and highest instantaneous luminosity for Run 1A are 0.54×10^{31} cm^{2}s^{-1} and 0.92×10^{31} cm^{2}s^{-1}, respectively. Similarly, for Run 1B, they are 1.6×10^{31} cm^{2}s^{-1} and 2.8×10^{31} cm^{2}s^{-1}, respectively. The measured integrated luminosity for Run 1A and Run 1B is 109±7 pb.

2.2.7 Trigger system

At the Tevatron, the rate of bunch crossings is about once every 3.5 μs. The total inelastic interaction rate of $p\bar{p}$ collision is about 600 kHz, using a $p\bar{p}$ total cross-

section of 60 mb [18] at $\sqrt{s}$ =1.8 TeV and a typical luminosity of 1.0×10^{31} $cm^{-1}s^{-}$ However, the CDF detector is only able to write write to a 8 mm tape up to 10 event per second. In this reason, trigger system for reducing an event rate is necessary. Th CDF trigger system consists of three levels [19, 20, 21]. The level 1-3 triggers consis of a logical OR of several requirements of electrons, photons, muons, missing energ jets, taus and select events based on physics interests.

The level 1 trigger is a dedicated electronics trigger. Its decision is based on th presence of an energy cluster above some energy threshold in the $\Delta\eta \times \Delta\phi = 0.2 \times 1$ trigger towers of calorimeters. It is also based on the presence of muon track segmen in the muon chambers. The decision is made within the 3.5 μs of bunch crossing tir not to make dead time. The level 1 trigger reduces the event rate to about a few kH The events that pass the level 1 trigger are delivered to the level 2 trigger processo

The level 2 trigger is an also a hardware trigger. A difference between level trigger is that it combines the data of several detector subsystems. The level 2 trig decisions are based on the presence of calorimeter energy clusters, missing transve energy in the calorimeters, stiff central tracks inside the CTC, and matching of C and level 1 muon chamber track stubs. The decision time per event is about 20 This causes about 5% dead time as events that come through level 1 triggers dur the level 2 decision time. The event rate out of level 2 is typically 20 - 25 Hz depend on the instantaneous luminosity. A level 2 trigger pass initiates a full detector read which takes of the order a few ms per event.

The level 3 trigger is a software trigger that reconstructs and examines the en event. It removes junk event from level 2 triggered events and group the events i some data sets for offline analysis. After passing the level 3 triggers, the data is stc on disk and spooled to the 8 mm tape. This analysis uses the high pt central elect data set and the high pt central muon data sets.

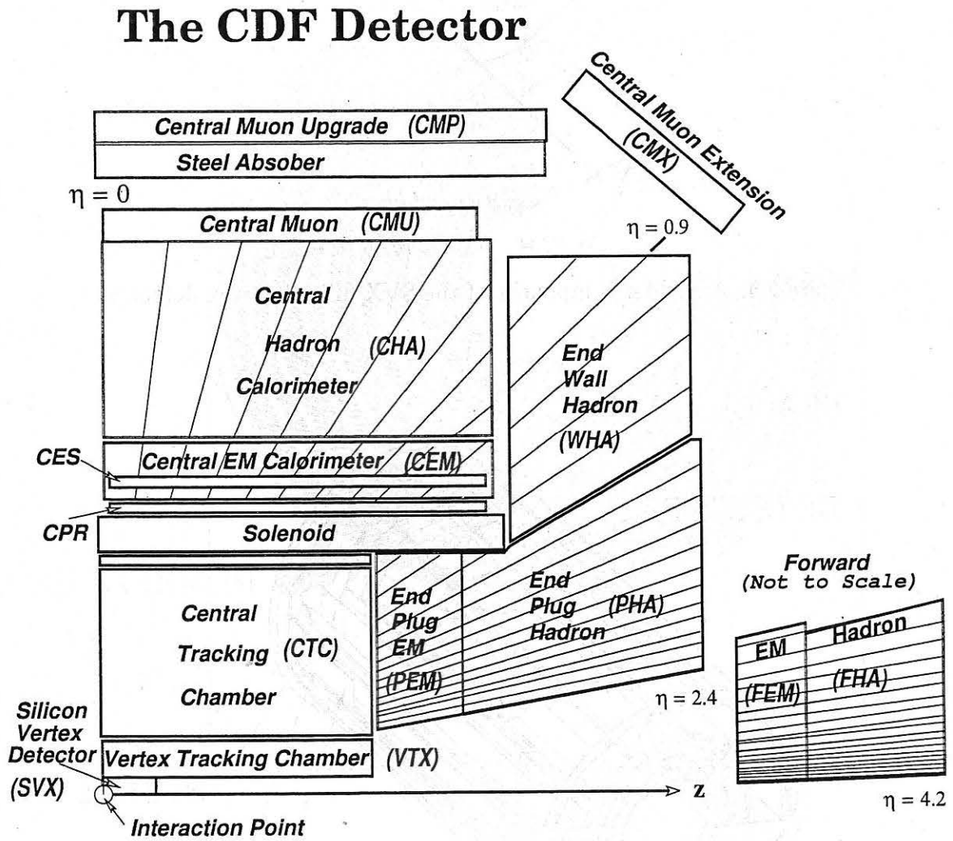

Figure 2.3: A quarter side view of the CDF

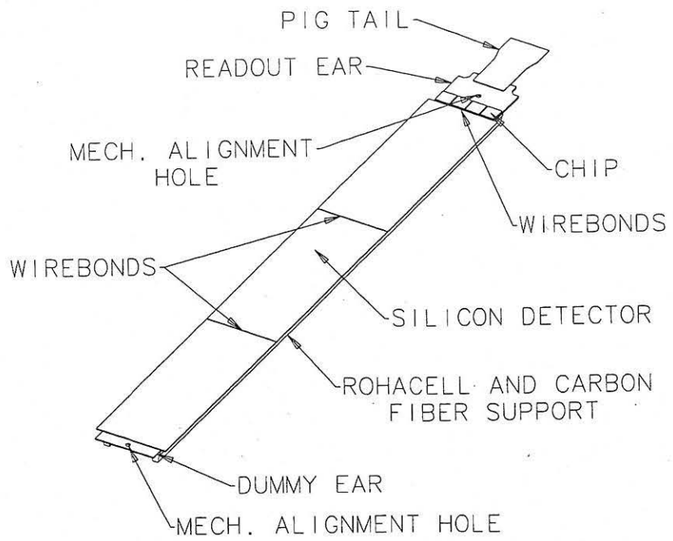

Figure 2.4: A Ladder component of the SVX Silicon vertex detector.

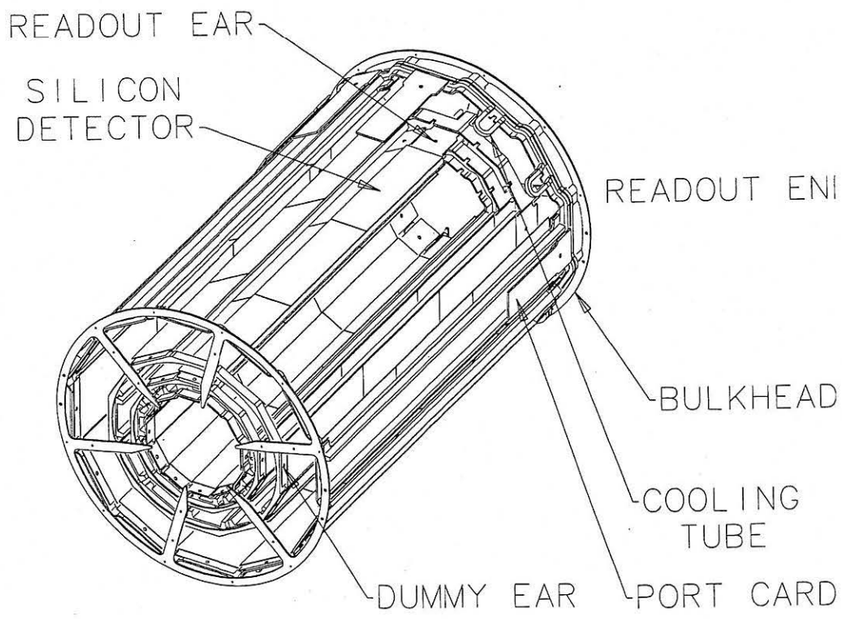

Figure 2.5: Layout of a barrel of the SVX Silicon vertex detector.

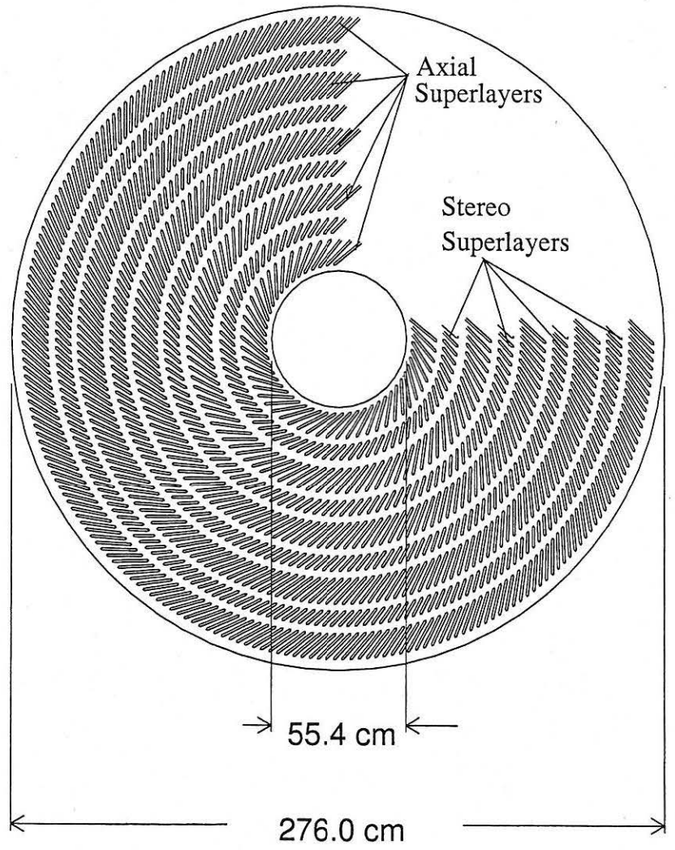

Figure 2.6: An endplate of the Central Tracking Chamber.

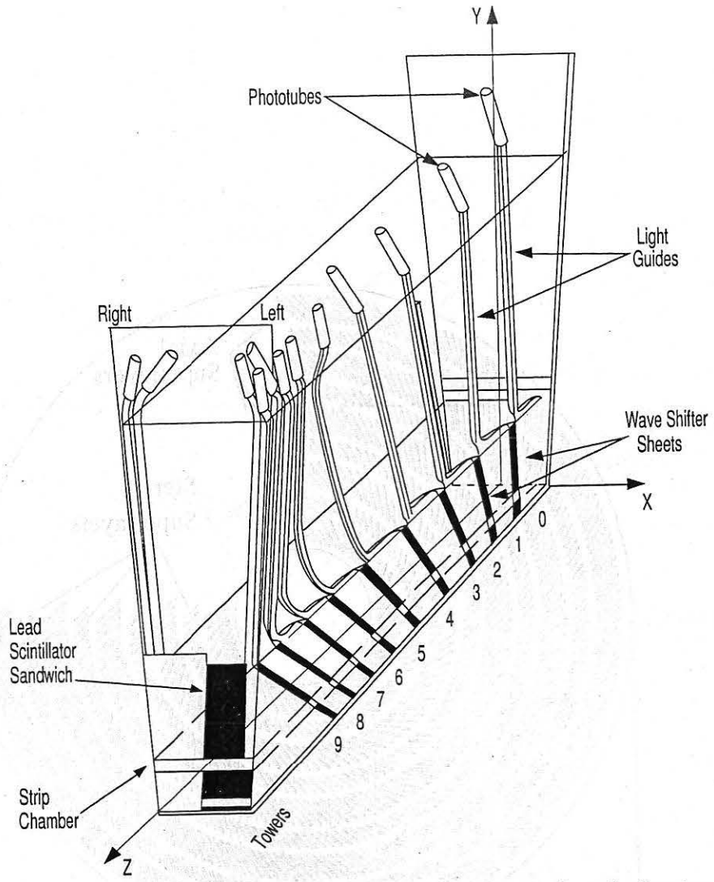

Figure 2.7: A wedge of the central electro magnetic calorimeter.

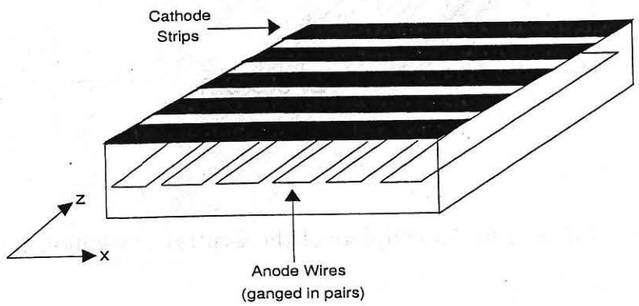

Figure 2.8: Schematic view of the central electro magnetic strip chamber.

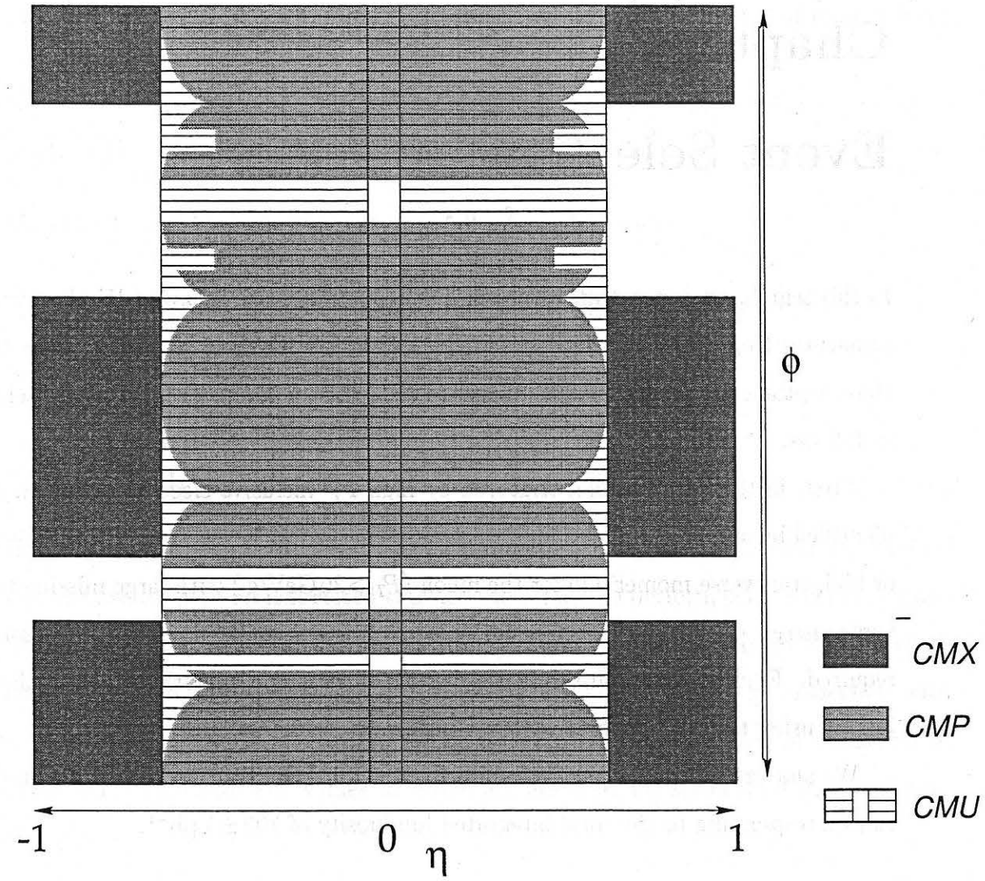

Figure 2.9: The $\eta - \phi$ muon coverage for the central region of the CDF detector. The ϕ gaps in the CMX coverage are where the CMX intersects the floor (large gap) and Tevatron components (small gap).

Chapter 3

Event Selection

In this search, we concentrate on looking at the leptonically decaying W plus two jet signatures from these two processes: $\rho_T^{\pm} \to W\pi_T^0 \to l\nu b\bar{b}$ and $\rho_T^0 \to W\pi_T^{\pm} \to l\nu b\bar{c}$ Here, leptonically means that W decays to $e\nu_e$ or $\mu\nu_\mu$. These final states are selecte as follows.

First, in the data samples triggered by high P_T inclusive electron or muon, W : identified by requiring isolated high transverse energy for the electron (E_T >20 GeV/c or high transverse momentum for the muon (P_T >20 GeV/c) with large missing tran: verse energy ($\not\!\!E_T$>20 GeV). Second, exactly 2 jets associated with a W boson a: required. Finally, we require that we identify at least one b-quark tagged in the tw jets by using the SVX detector (SVX b-tag).

We analyze all the data collected during 1992-93 run (Run 1A) and 1994-96 (Ru 1B) corresponding to the total integrated luminosity of $109 \pm 7\,\mathrm{pb}^{-1}$.

3.1 Transverse Momentum and Energy

A transverse momentum (P_T) and a transverse energy (E_T) are defined by

$$P_T = P \sin\theta, \tag{3.}$$

$$E_T = E \sin\theta, \tag{3.}$$

where P is the three momentum measured in the central calorimeter, E is the energy measured in the calorimeter, and θ is the scattering angle in the laboratory system.

These transverse variables are useful at the high energy proton anti-proton colliding experiment because they are Lorenz invariant variables in any center of mass system of the elementary process.

3.2 W Boson Selection

To select W samples, events must pass following selections:

1. Must has a good isolated high P_T electron or muon (see section 3.1.1).
2. Must passes Z^0 veto (see section 3.1.2).
3. $\not\!\!E_T > 20$ GeV (see section 3.1.3).

3.2.1 High E_T Electron Selection

High E_T electrons are identified by the large energy deposit in the EM calorimeter and the existence of an associated track in the CTC. We perform some electron identification cuts described below to remove the background such as charged hadron which deposits a lot of energy in the EM calorimeter and γ or γ's from π^0 associated with a CTC track from a charged hadron. Cut values for electrons are summarized in Table 3.1. The tight cut values in Table 3.1 are used for selecting a good primary electron.

- Electron clustering

  Electron identification begins with a clustering algorithm to identify electron showers. An electron cluster consists of a seed tower (the tower in the cluster with the largest energy) and shoulder towers (adjacent towers incorporated into the cluster). Towers with electromagnetic(EM) transverse energy E_T > 3 GeV are

eligible to be seed towers. Towers with EM $E_T > 0.1$ GeV are eligible to b shoulder towers. The maximum cluster size is restricted to three towers in pse dorapidity ($\Delta\eta \approx 0.3$) by one tower in azimuth ($\Delta\phi \approx 15^o$) in the central regi $|\eta| < 1.1$.

- $E_T >$ 20 GeV
  Transverse energy deposited in CEM calorimeter. The fraction of hadron je falsely identified as electrons is estimated to be 2×10^{-5} for jets with E_T 20 GeV [22].

- $E/P < 1.8$
  The ratio of the electron's energy in the CEM calorimeter (E) to its momentu from the CTC track (P). The E/P value of the electron must be around 1.

- $Had/EM < 0.05$
  The ratio of the energy in the hadronic section (Had) to the energy in the el tromagnetic section (EM). Isolated electrons would have less hadronic ene nearby them than hadronic jets includes electrons such as semi-leptonic b dec

- $L_{shr} < 0.1$
  The lateral energy sharing in an electron cluster between the CEM tower w the most of the energy and the adjacent towers, defined as

$$L_{shr} = 0.14 \sum \frac{E_i^{adj} - E_i^{prob}}{\sqrt{0.14^2 E + (\Delta E_i^{prob})^2}} \qquad (1$$

  where E_i^{adj} is the measured energy (in GeV) in the i-th tower adjacent to the s tower, E_i^{prob} is the expected energy (in GeV) in the i-th adjacent tower, 0.14 (in GeV) is the error on the energy measurement, and ΔE_i^{prob} (in GeV) is error on the energy estimate. The E_i^{prob} is calculated by using the test b result.

- $|\Delta x| < 1.5$ cm, $|\Delta z| < 3.0$ cm
  The position matching between CTC track position to the electron cluster and the shower position measured in the CES strip chamber. The $|\Delta x|$ and $|\Delta z|$ are the separation in the x direction and in the z direction respectively. These cuts reduces backgrounds from chance overlap of charged particles and γ or π^0.

- $\chi^2_{strip} < 10$
  The fitting χ^2 of the energy deposited along the z strips in the CES compared to the test beam data.

- $|Z_\nu| <$60 cm
  The z-position of the primary $p\bar{p}$ collision vertex. It is measured by the vertex tracking chamber (VTX). The interaction z-positions are distributed by Gaussian shape with standard deviation $\sigma \sim$30 cm. The primary vertex should be within 2σ in the z-direction.

- $|Z_\nu - Z_0^e| < 5.0$ cm
  The Z-vertex matching between the the primary vertex and the primary electron vertex is within 5.0 cm. This makes sure that the event vertex is determined correctly in the environment of high instantaneous luminosity.

- Electron fiducial cut
  The fiducial volume for electrons covers 84 % of the solid angle in the region $|\eta| <$ 1.0 . The electron position is required to be away from calorimeter boundaries so that the electron shower is fully contained in the active region.

- Conversion removal
  Electrons from photon conversions have to be removed from the electron sample. The conversion electrons can be identified with a high efficiency of $(88 \pm 4)\%$ [23] using tracking information. Any electron that does not have a matching VTX

Variable		Tight Cut	Loose Cut
Calorimeter	:	CEM	CEM,PEM,FEM
E_T	:	> 20 GeV/c^2	> 10 GeV/c^2
E/P	:	< 1.8	> 2.0 (if CEM)
$Had/EM(3\times 3)$	:	< 0.05	< 0.12
L_{shr}	:	< 0.1	-
$\lvert\Delta x\rvert$	:	< 1.5 cm	-
$\lvert\Delta z\rvert$	:	< 3.0 cm	-
$\lvert Z_\nu - Z_0^e\rvert$	:	< 5.0 cm	-
$\lvert Z_\nu\rvert$	:	< 60.0 cm	-
χ^2_{strip}	:	< 10.0	-
Fiducial Cuts on the Electrons	:	FID_ELE=0	-
Conversion Removal	:		-
Calorimeter Isolation (Cone 0.4)	:	< 0.1	< 0.2

Table 3.1: List of the electron selection cut value.

track, or that can be paired with an oppositely charged CTC track to form small effective mass, is rejected as a photon conversion.

- $I^e_{cal}(0.4) < 0.1$

  The calorimeter isolation within a cone of radius $R = \sqrt{(\Delta\phi)^2 + (\Delta\eta)^2} =$ around the electron. This remove background from leptonically decayed hea flavor jets. $I^e_{cal}(0.4)$ is defined by as:

$$I^e_{cal}(0.4) = \frac{E_T(0.4) - E^e_T}{E^e_T} \qquad (3$$

  where $E_T(0.4)$ is the total transverse energy in a cone radius R=0.4 and E^e_T the electron transverse energy.

3.2.2 High P_T Muon Selection

High P_T muons are identified by the muon chamber hits associated with a CTC tr with a consistent energy deposit in the calorimeter as a minimum ionizing parti Following cuts are applied to reduce the background such as cosmic rays and char hadron which punch through the calorimeters and leave a track in the muon chamb

Cut values for muons are summarized in Table 3.2. In the table, tight cut values are used for selecting a good primary muon. The primary muon represents the highest P_T muon which go through the tight muon cuts.

- $P_T >$ 20 GeV with a CMU or CMP or CMX track.

  Transverse momentum measured by the CTC track associated with a muon chamber track in CMU or CMP or CMX.

- EM Energy < 2.0 GeV , Had Energy < 6.0 GeV , EM+Had Energy > 0.1 GeV

  The deposit energy in the EM calorimeter tower and the Had calorimeter tower corresponding to the CTC track. They are required to be consistent with a minimum ionizing particle.

- Impact Parameter < 0.3 cm

  The distance on the r-ϕ plane between beam line and the muon track extrapolated from the track by CTC and SVX information. This cut reduces cosmic ray background and the muon from the decay in flight.

- $\lvert Z_\nu\rvert < 60.0$ cm

  The z-position of the primary $p\bar{p}$ collision vertex. It is measured by the vertex tracking chamber (VTX). The interaction z-positions are distributed by Gaussian shape with standard deviation $\sigma \sim$30 cm. The primary vertex should be within 2σ in the z-direction.

- $\lvert Z_\nu - Z^\mu_0\rvert < 5.0$ cm

  The Z-vertex matching between primary event z-vertex and the primary muon z-vertex. This makes sure that the event vertex is determined correctly in the environment of high instantaneous luminosity. This also removes cosmic ray background.

Variable		Tight Cut	Loose Cut
Muon Chamber	:	CMU,CMP,CMX	CMU,CMP,CMX,CMIO
P_T	:	> 20 GeV/c	> 10.0 GeV/c
EM Energy	:	< 2.0 GeV	< 5.0 GeV ; < 2.0 GeV (CMIO)
Had Energy	:	< 6.0 GeV	< 10.0 GeV ; < 6.0 GeV (CMIO)
Had+EM Energy	:	> 0.1 GeV	-
Impact parameter	:	< 0.3 cm	-
$\lvert Z_\nu - Z_0^\mu \rvert$	:	< 5.0 cm	-
$\lvert Z_\nu \rvert$	:	< 60.0 cm	-
$\lvert \Delta x \rvert$	:	< 2.0 cm (CMU)	< 5.0 cm (CMU)
		.or. < 5.0 cm (CMP)	*.or.* < 5.0 cm (CMP)
		< 5.0 cm (CMX)	< 5.0 cm (CMX)
Calorimeter Isolation			
(Cone 0.4)	:	< 0.1	< 0.2
$\lvert \eta \rvert$	:	-	< 1.2 (CMIO)

Table 3.2: List of the muon selection value.

- $|\Delta x| < 2.0\,\text{cm}$ (CMU) *.or.* $< 5.0\,\text{cm}$ (CMP) *.or.* $< 5.0\,\text{cm}$ (CMX)

  The difference between the position in X of the reconstructed muon stub in t muon chamber and the extrapolated CTC track. These cuts reduces backgrour from accidental overlap of muon chamber hits from cosmic rays and a CTC tr from a charged particle.

- $I^{\mu}_{cal}(0.4) < 0.1$

  The calorimeter isolation of the muon within a cone of radius $R = 0.4$ aro the muon. This removes background from leptonically decayed heavy flavor j $I^{\mu}_{cal}(0.4) < 0.1$ is defined by as:

$$I^{\mu}_{cal}(0.4) < 0.1 = \frac{E_T(0.4) - E_T^{\mu\ tower}}{P_T^{\mu}} \qquad (3$$

  where $E_T(0.4)$ is the energy in a cone radius R=0.4, $E_T^{\mu tower}$ is the transverse ergy deposited in the tower traversed by the muon and P_T^{μ} the muon moment

3.2.3 Z^0 Veto

We apply the cut on the invariant mass of two electrons or two muons within 75GeV/c^2 to 105 GeV/c^2 so as to remove Z^0 particle. This removal reduces background events including Z^0 such as ZZ, WZ, and $Z^0 + b\bar{b}$ QCD processes.

A primary lepton is selected by the criteria described above. The second leg leptons are identified using loose cuts listed in table 3.1 and table 3.2. We select CMIO(Central Minimum Ionizing) particles as a second leg muons in the central region without going through the muon chamber fiducial region.

Loose electron cuts

Loose electron cuts are used to identify the second leg electron associated with high E_T electron from Z^0 decay.

- E_T> 20 GeV in CEM or PEM or FEM
- $Had/EM < 0.12$
- $E/P < 2.0$ (only for CEM)
- $I^{e}_{cal}(0.4) < 0.2$

Loose muon cuts

Loose muon cuts are used to identify the second leg muon associated with high P_T muon from Z^0 decay.

- P_T> 10 GeV with a CMU or CMP or CMX track.
- EM Energy < 5.0 GeV Had Energy < 10.0 GeV
- $|\Delta x| < 5.0\,\text{cm}$ (in any muon chamber)

- $I^{\mu}_{cal}(0.4) < 0.2$

CMIO cuts

CMIO (Central Minimum Ionizing particles) cuts are used to identify a second l muon with no muon chamber track associated with high P_T muon from Z^0 decay.

- Muon chamber track is not required.
- $|\eta| < 1.2$
- $P_T >$ 10 GeV
- EM Energy < 2.0
- Had Energy < 6.0
- $I^{CMIO}_{cal}(0.4) < 0.2$

3.2.4 Neutrino identification using Missing E_T

A high P_T neutrino is expected from the decay of W. However, the neutrino g through CDF detector without interacting. The neutrino is detected by the prese of a large transverse momentum imbalance ("*missing* E_T or $\not\!\!E_T$"). Here, we use o transverse information because the beam axis momenta of the initial partons in proton and anti-proton are not identified. The missing E_T is calculated from

$$\not\!\!E_T \equiv \left|(-1) \times \sum \vec{E}^i_T\right|, \qquad (3$$

where $\vec{E}^i_T$ is a transverse energy vector whose magnitude is the transverse energy a calorimeter tower and whose direction points from the event vertex to the cente the calorimeter tower. The transverse energy vector is summed up within the re $|\eta| < 3.6$.

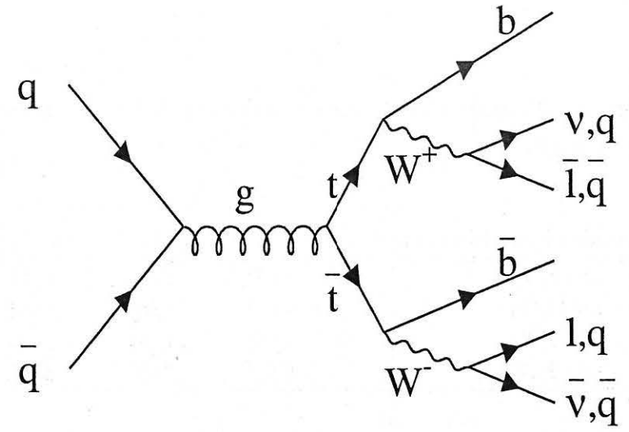

Figure 3.1: One of the leading order feynman diagram for $t\bar{t}$ production.

The uncertainty of the missing E_T measurement depends on scalar sum of the calorimeter E_T(sum E_T). The dependence is measured from CDF minimum bias data (requires only BBC hits), and it is expressed as,

$$\sigma(\not\!\!E_T) = -0.58 + 0.742\sqrt{(\text{sum}E_T)} \qquad (3.7)$$

where the $\sigma(\not\!\!E_T)$ is the uncertainty of the missing E_T. On the sum E_T typical of technicolor W plus two jet events, the $\sigma(\not\!\!E_T)$ is on the order of 6 GeV , while the neutrino P_T from a W is on the order of 20-40 GeV . For selecting W, we require the missing E_T greater than 20 GeV . This $\not\!\!E_T$ cut discriminates technicolor event with 3 σ level from the background without W boson.

3.2.5 $t\bar{t}$ candidates removal

We apply dilepton removal to eliminate $t\bar{t}$ dilepton events. In the framework of the standard model, a t quark decays mostly to a W and a b quark. In $t\bar{t}$ pair production events, the $t\bar{t}$ decays to two Ws and two b quarks. As shown in Figure 3.1, the two Ws decay either to a lepton and a neutrino, or a quark and an anti-quark. The quarks hadronize to make jets. The branching ratio for the various decay modes are listed in

Table 3.3. Here we eliminate the $t\bar{t}$ events that both of the Ws decay to electron or muon.

W Decay mode (Branching ratio)	$e\nu$ (1/9)	$\mu\nu$ (1/9)	$\tau\nu$ (1/9)	$q\bar{q}$ (2/3)
$e\nu$ (1/9)	1/81	1/81	1/81	6/81
$\mu\nu$ (1/9)	1/81	1/81	1/81	6/81
$\tau\nu$ (1/9)	1/81	1/81	1/81	6/81
$q\bar{q}$ (2/3)	6/81	6/81	6/81	36/81

Table 3.3: Decay modes of W and the branching ratio of a $t\bar{t}$ pair production. The symbol q stands for a light quark: u, d, c, s.

We use same dilepton selection method as in the $t\bar{t}$ dilepton decay mode search at the CDF [24]. In the dilepton $t\bar{t}$ cut, opposite charged high P_T ee, $\mu\mu$, or $e\mu$ events with $\not\!\!E_T$>25 GeV are required, and also $\delta\phi(\not\!\!E_T, j) > 20^o$ and $\delta\phi(\not\!\!E_T, l) > 20^o$ are required if $\not\!\!E_T < 50$ GeV , where the $\delta\phi(\not\!\!E_T, j)$ is the azimuthal angle between the direction of $\not\!\!E_T$ and the direction of the nearest isolated high P_T lepton, and the $\delta\phi(\not\!\!E_T, j)$ is the azimuthal angle between the direction of $\not\!\!E_T$ and the direction of the nearest jet having $E_T > 10$ GeV . Azimuthal angle cuts mainly reduce $Z \to \tau\tau$ background. Detail of the $t\bar{t}$ dilepton selection is described in [24].

3.2.6 Selected W events

After all selection cuts discussed above, a total number of 68874 electron and 4483(muon events remain in the CDF data. Figure 3.2 shows the transverse mass distributior from a lepton and $\not\!\!E_T$ system for the electron and muon samples. A clear Jacobiar peak is observed at the W mass, around 80 GeV/c^2 .

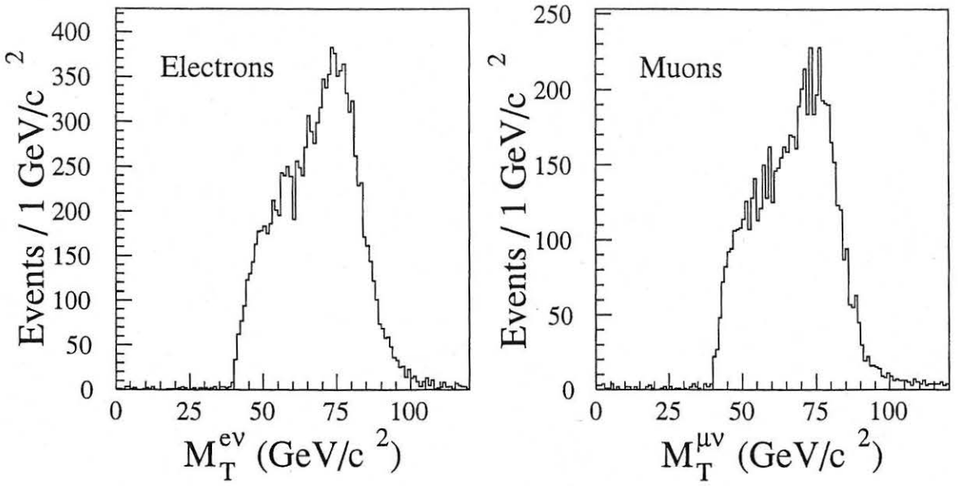

Figure 3.2: M_T Distributions of the W boson selected sample in the CDF data for the electron mode and for the muon mode.

3.3 Jet Selection

Hard scattered quarks and gluons produce the collimated sprays of particles, which are called 'jets'. Jets observed in the detector are hadrons which are created through the fragmentation process of quarks and gluons. The experimental signature of a jet is a large energy deposit in a localized area of the detector. At the CDF experiment, jets are reconstructed using a fixed cone algorithm. A detailed description of the algorithm can be found in reference [25]. The algorithm forms clusters from the energies deposited in the calorimeter towers within a fixed cone radius $R < R_0$. The radius $R_0 = 0.4$ is used for this analysis.

In this analysis, jets are retained if they have $E_T > 15$ GeV and $|\eta| < 2.0$. The jet E_T and $|\eta|$ are calculated using lepton z vertex information. We require exactly 2 jets in our W selected sample to separate technicolor events from $t\bar{t}$ production events. Events with three or more jets associated with W contain large amount of $t\bar{t}$ events [24].

3.4 Dilepton Removal Using Track Information.

In the W + 2 jet sample, we apply one more dilepton removal using CTC track information. This cut can eliminate τ type decay mode from the $t\bar{t}$ production. From the $t\bar{t}$ monte carlo study, this cut is expected to remove about 25 % of the remaining $t\bar{t}$ dilepton events satisfying the W+ 2 jet signature. We remove events with a high P_T (>15 GeV/c) isolated track and opposite charge from the primary lepton charge. The track isolation requires $\Sigma P_T < 2.0$ GeV/c in the cone of 0.4 around the candidate track.

3.5 SVX b Quark Tagging

The background event rate of the W + 2 jet is still more than 30 times larger than the technicolor signal event rate. This ratio can be considerably improved by requiring at least one out of the two selected jets to be identified as a b quark jet by the SVX detector. The long lifetime of B hadrons ($c\tau \sim 450\mu$m) [26] and the high Q value of the heavy technipion decay boost the B hadrons to travel measurable distance from the primary vertex before decaying. The secondary vertices from B hadron decay is detected using the Silicon Vertex Detector.

- Loose definition of a displaced track
  - $P_T > 0.5$ GeV/c in the jet cone of $R = 0.4$.
  - Impact parameter significance $|S_{d0}| > 2.5$.
  - At least 1 good cluster for 3 or 4 hit tracks.
  - $P_T > 1.5$ for 2 hit tracks.
- Tight definition of a displaced track
  - $P_T > 1.5$ GeV/c in the jet cone of $R = 0.4$.

  - Impact parameter significance $|S_{d0}| > 4$.
  - At least 1 good cluster for the 4 hit tracks.
  - At least 2 good cluster for the 3 hit tracks.

The vertices with three or more tracks with loose track requirements are searched at first. If the first attempt fails, the two-track vertices are tried to be reconstructed by using more stringent track and vertex quality criteria. To find the stringent tracks, we require that these particles lie within a cone radius $R = 0.4$ around the jet axis. Since the tracks with $P_T < 0.4$ GeV curl in the CDF magnetic field and tend to be poorly measured, we only consider tracks with $P_T > 0.5$ GeV . The impact parameter significance ($|S_{d0}| = d_0/\sigma_{d_0}$) of the track is required to be larger than 2.5, where the d_0 is the impact parameter of the track from the primary vertex in the r-ϕ plane. It is schematically shown in Figure 3.3. The σ_{d_0} is the uncertainty of the impact parameter measurement, and it is defined as:

$$\sigma_{d0} = \sqrt{10^2 + 13^2 + (60/P_T)^2} \ \mu m \ . \tag{3.8}$$

Finally, at least one good hit cluster is required for the three hit and four hit tracks. The good hit cluster is a 3 or less strips long continuous cluster and without including bad strips. Here, three hit and four hit is the number of hit in the four layer of the SVX detector. For the 2 hit track, the good cluster is not required. However, the P_T cut is more strict, $P_T > 1.5$ GeV .

Finally for all secondary vertex candidates, the 2D decay length on the x-y plane L_{xy} and its error σ_{xy} are calculated from the constrained vertex fit. A b-tag is required to have:

- $\frac{|L_{xy}|}{\sigma_{L_{xy}}} > 3.0$
- $|L_{xy}| < 5.0$cm .

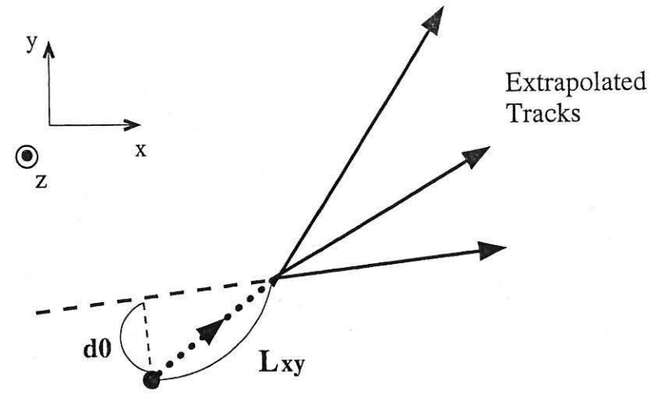

Figure 3.3: Schematic of the SVX b-tag. The long L_xy is a signal of the b quar production. The L_xy is measured in the x-y plane of the detector. We identify th tracks associated with the secondary vertex by requiring a large impact parameter, d with respect to the interaction point.

Data	Number of events (electron/muon)
W selection	113710 (68874/44836)
W + 2 jet	1611 (904/707)
SVX b-tag	42 (24/18)

Table 3.4: Number of data events after W selection, W + 2 jet selection, and at lea one SVX b-tagged W + 2 jet selection.

The maximum L_{xy} is set not to mis-identify K^0_{short} decay vertex or other fake vert as a b-quark jet.

After the b-tag requirement, 42 events are selected from 109 pb^{-1} of the CDF dat Event statistics in our selection process is summarized in Table 3.4.

Chapter 4

Signal Acceptances

This chapter describes the estimation of the signal efficiency. The signal efficiency is used to estimate an expected number of technicolor signal events and the cross section upper limit which will be described in chapter 8. The signal efficiency of the W+2jet and b-tag selection is described in this chapter. Total efficiencies including additional topology and mass window selection criteria are shown in chapter 8.

4.1 Monte Carlo Event Generator

We use the PYTHIA version 6.1 Monte Carlo generator program which includes walking technicolor processes as described in [9]. Using PYTHIA 6.1, we generated ρ_T^0 and $\rho_T^\pm$ at $\sqrt{s} = 1.8$ TeV $p\bar{p}$ collisions. The selected signatures are the followings:

$$
\begin{array}{lll}
q\bar{q} \to W^{*\pm} \to \rho_T^\pm \to W^\pm \pi_T^0 & (\pi_T^0 \to b\,\bar{b} : 100\,\%) & (\text{W force to } e\nu, \mu\nu) \\
q\bar{q} \to Z^{0*}, \gamma^* \to \rho_T^0 \to W^\pm \pi_T^\mp & (\pi_T^\pm \to b\,\bar{c}, c\,\bar{b} : 95\,\%) & \\
 & (\pi_T^\pm \to c\,\bar{s}, s\,\bar{c} : 5\,\%) & (W \text{ force to } e\nu, \mu\nu)
\end{array}
$$

We generated 10k events at each π_T,ρ_T mass combination. Mass combinations are chosen by looking at the cross section contour plot (Figure 1.7). The mass combinations whose cross section is more than 5 pb are chosen.

Mass Combination [M(π_T),M(ρ_T)]

[80,165] [80,170] [80,180]

[84,165] [84,168] [84,175]

[85,168] [85,170] [85,175] [85,180]

[90,173] [90,175] [90,180] [90,185] [90,190]

[95,178] [95,180] [95,185] [95,190] [95,195]

[100,183] [100,185] [100,190] [100,195] [100,200] [100,205] [100,210]

[105,188] [105,190] [105,195] [105,200] [105,205] [105,210]

[110,193] [110,195] [110,200] [110,205] [110,210] [110,220]

[115,198] [115,200] [115,205] [115,210] [115,215]

[120,210] [120,220] [120,230]

4.2 Acceptances

The total acceptance is defined as the fraction of signal events that pass all the selection requirements. It can be factorized as:

$$\varepsilon_{W+2jet\,b\text{-}tag} = A_{kin,geom} \cdot \varepsilon_{trig} \cdot \varepsilon_{lepton_{ID}} \cdot \varepsilon_{dil,Z^0\,removal} \cdot \varepsilon_{b-tag} \cdot SF_{ID} \cdot SF_{b-tag}$$

where

- $A_{kin,geom}$: A_{l_fid} , $A_{E_{T_l}}$, A_{l_iso} , $A_{\not\!\!E_T}$, $A_{2\ jet}$, and A_{zvtx}
  - A_{l_fid} : fiducial acceptance for leptons
  - $A_{E_{T_l}}$: lepton transverse energy $E_T > 20$ GeV
  - A_{l_iso} : lepton isolation $Iso(0.4) < 0.1$
  - $A_{\not\!\!E_T}$: $\not\!\!E_T$ >20 GeV
  - $A_{2\ jet}$: exclusive 2 jet selection described in Section 3.5
  - A_{zvtx} : z vertex cut $|z|$ <60 cm

	Central electron	Central muon	CMX muon
$\varepsilon_{ID}(1B)$	0.818	0.942	0.952
$\varepsilon_{ID}(1A)$	0.849	0.921	0.951

Table 4.1: Lepton ID efficiencies.

- ε_{trig} : trigger efficiency
- $\varepsilon_{lepton_{ID}}$: lepton ID efficiency
- $\varepsilon_{dil,Z^0\,removal}$: $t\bar{t}$, Z^0, and extended dilepton removal efficiency
- ε_{b-tag} : b-tag efficiency

We assumed the electron trigger efficiency to be fully efficient [?]. SIMMUTRIG trigger simulation efficiency is used for muons.

In addition, we applied the scale factor of the lepton ID efficiency (SF_{ID}). Lepton ID scale factor is the fraction of the lepton ID efficiency in the data and in Monte Carlo. The lepton ID efficiency for the data is derived using the Z^0 data, by examining one leg of the dilepton system [?]. These values are summarized in Table 4.1. Mathematically this can be written as:

$$SF_{ID} = \frac{\varepsilon_{l_{ID}}^{data}}{\varepsilon_{l_{ID}}^{MC}}$$

Finally, we applied scale factor to the SVX b-tag efficiency (SF_{b-tag}). It is computed by comparing the single b-tag efficiencies of the degraded SVX b-tag routine and the standard SVX b-tag routine:

$$SF_{b-tag} = \frac{\varepsilon_{b-tag}^{MCdegrade}}{\varepsilon_{b-tag}^{MC}}$$

The total efficiencies in every mass combinations are summarized in Table 4.2. The cross section, and the expected number of signal for 109 pb^{-1} are also in Table 4.2. Acceptance and efficiencies are plotted in Figure 4.1.

$M(\pi_T)$,$M(\rho_T)$ [GeV/c^2]	σ	$\varepsilon_{W+2jet\,b\text{-}tag} \cdot BR(W \to e,\mu)$	$N_{expected}(109\,pb^{-1})$
80,165	4.2 pb	0.73 %	3.3 events
80,170	4.1 pb	0.78 %	3.5 events
80,180	3.1 pb	0.74 %	2.5 events
85,170	15.4 pb	0.87 %	14.6 events
85,175	7.5 pb	0.75 %	6.1 events
85,180	5.1 pb	0.80 %	4.4 events
90,175	12.9 pb	0.93 %	13.1 events
90,180	17.6 pb	0.85 %	16.4 events
90,185	8.4 pb	0.89 %	8.1 events
95,180	10.7 pb	1.06 %	12.4 events
95,185	14.2 pb	1.03 %	15.9 events
95,190	13.8 pb	0.93 %	13.9 events
100,190	12.0 pb	1.11 %	14.5 events
100,195	12.0 pb	0.99 %	12.9 events
100,200	10.9 pb	0.95 %	11.3 events
105,195	10.1 pb	1.11 %	12.2 events
105,200	10.4 pb	1.10 %	12.5 events
105,205	9.3 pb	0.99 %	10.0 events
110,200	8.4 pb	1.12 %	10.2 events
110,205	8.9 pb	1.14 %	11.0 events
110,210	8.1 pb	1.07 %	9.5 events
115,205	7.2 pb	1.23 %	9.7 events
115,210	7.7 pb	1.17 %	9.8 events
115,215	7.2 pb	1.11 %	8.7 events

Table 4.2: Production cross sections times branching ratio of $\rho_T^{\pm} \to W^{\pm} + \pi_T^0$ a
$\rho_T^0 \to W^{\pm} + \pi_T^{\mp}$ (σ), total efficiencies of the W + 2 jet b-tag selection ($\varepsilon_{W+2jet\,b\text{-}tc}$
including BR($W \to e,\mu$), and expected number of signal events for 109 pb^{-1}.

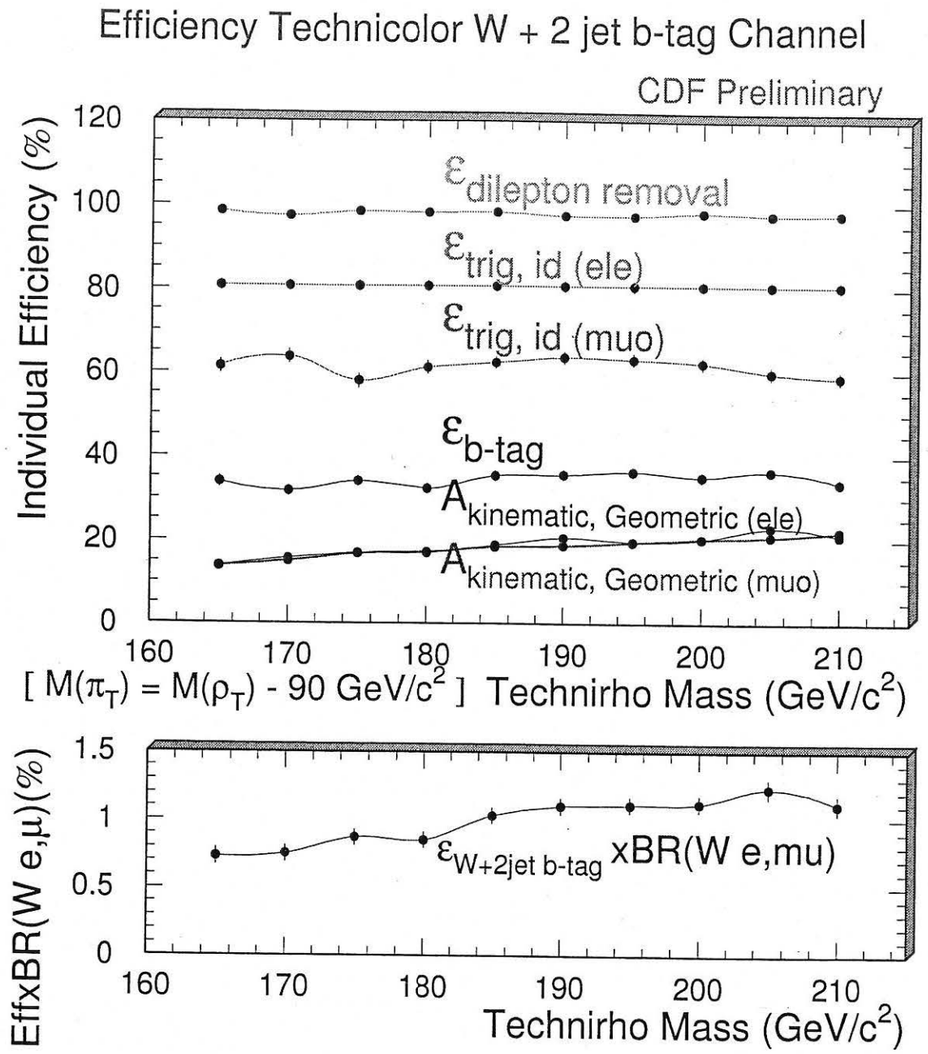

Figure 4.1: Acceptances, efficiencies of each cut, and total efficiencies of the W + 2 jet b-tag selection ($\varepsilon_{W+2jet\,b\text{-}tag}$) including BR($W \to e,\mu$) as a function of the Technirho mass. Technipion mass is fixed to $M(\rho_T) - 90$ GeV/c^2 .

Chapter 5

Background Estimation

In this chapter, we describe the background estimation for SVX b-tagged W plus two jets events. We finally expect 31.6 ± 4.3 background events in our sample from a variety of sources from the simulation study described below. The background sources are events from the production of a W in association with heavy quark pairs ($Wb\bar{b}, Wc\bar{c}$) [27], $t\bar{t}$ production, b-quark mistag due to track mismeasurements, $p\bar{p} \rightarrow W+$ charm, QCD, diboson production, $Z \rightarrow \tau\bar{\tau}$, Z plus heavy flavor(h.f.), and single top production. The expected number of events of these backgrounds are computed separately for an individual process by using Monte Carlo program. They are summarized in Table 5.1. The dominant contribution to the background is expected to come from the $Wb\bar{b}, Wc\bar{c}$.

We use the kinematical and mass distributions of each background source for further analysis as discussed in the following chapters. The Monte Carlo programs used to make the event distributions are also listed in Table 5.1. The mistag and the QCD background distributions are obtained from CDF data. In the following sections, we describe the detail of the estimation for the each background source.

Source	Distribution	N_{event} ($109\,pb^{-1}$)
Mistag	Data ($W+$ 2 jet)	5.1±2.0
Wbb, Wcc	HERWIG	9.4±2.5
Z+h.f.	VECBOS	1.4±0.5
Wc	HERWIG	4.6±1.5
$WW, WZ, Z\tau\tau$	PYTHIA	1.5±0.5
QCD	Data ($\not\!\!E_T$,Iso method)	2.1±1.3
$t\bar{t}$	HERWIG (σ=7.5 pb)	5.1±1.9
single top	HERWIG (W^* and Wg)	2.4±0.8
TOTAL		31.6±4.3

Table 5.1: Expected number of background of W + 2 jet with b-tag selection for $109\,pb^{-1}$. The Monte Carlo generators (or data) used for obtaining mass and topological distributions are written in the 'Distribution' column.

5.1 QCD Background

The QCD background comes from the QCD jets production processes which fakes leptonic W boson decay events without including real W boson. The QCD background originates from two sources. One is the light quark or gluon QCD jets event and the other is the heavy quark(b or c) QCD jets event. One example for the light quark or gluon QCD jets, one lepton can be identified in the jet and the jet with large missing E_T because of the energy mismeasurement is slipped into the W selection criteria. The other example of the heavy quark(b or c) jets is that a heavy quark decays semi-leptonically and the lepton happens to be identified as an isolated high P_T lepton, and the missing E_T can be large because of the energy mismeasurement or because of the neutrino from the semi leptonic b or c quark decay.

We calculate the number of QCD background in the W+2jet events before b-tag and after b-tag separately. The QCD background before b-tag is used to measure the QCD background fraction in order to measure the number of W plus heavy flavor

background. To estimate the QCD background in our sample, we use the lepton isolation versus $\not\!\!E_T$ method. We divide the Isolation vs. $\not\!\!E_T$ plane in four differen regions.

- region A : $\not\!\!E_T$ < 15 GeV and Lepton Isolation < 0.1
- region B : $\not\!\!E_T$ < 15 GeV and Lepton Isolation > 0.4
- region C : $\not\!\!E_T$ > 20 GeV and Lepton Isolation > 0.4
- region D : $\not\!\!E_T$ > 20 GeV and Lepton Isolation < 0.1 (W signal region)

The definition of the 'Lepton Isolation' is defined in Section 3.1 for the electron an the muon separately. Under the assumption that the lepton Isolation and large $\not\!\!E_T$ ar independent process for QCD background events, we can estimate the contribution c the QCD background in the W signal region(D) using the number of events in eac region. The fraction of the QCD events in the signal region, F_{QCD}, is calculated usin following equation:

$$F_{QCD} = \frac{(N_A \times N_C)/N_B}{N_D} \quad (5.1$$

where N_X is the number of events in the region X.

Figure 5.1 shows the Missing E_T vs. Isolation plot of the CDF W+2jet data sampl before b-tag. Figure 5.2 shows the similar plot after b-tag. The same selection cut are applied as the described in Chapter.3 except for requiring the lepton isolation an the missing E_T. In table 5.2, the summary of the number of events survived in eac region and the estimated QCD fraction in the W+2jet selected data are listed befor b-tag. In table 5.3, same variables are listed for W+2jet with b-tag selection. Tabl 5.2 and 5.3 summarize the number of events in each region and the calculated result c the fraction of the QCD background in the CDF W+2jet data before and after b-ta The expected number of events in the 109 pb^{-1} of the CDF data is summarized i table 5.4

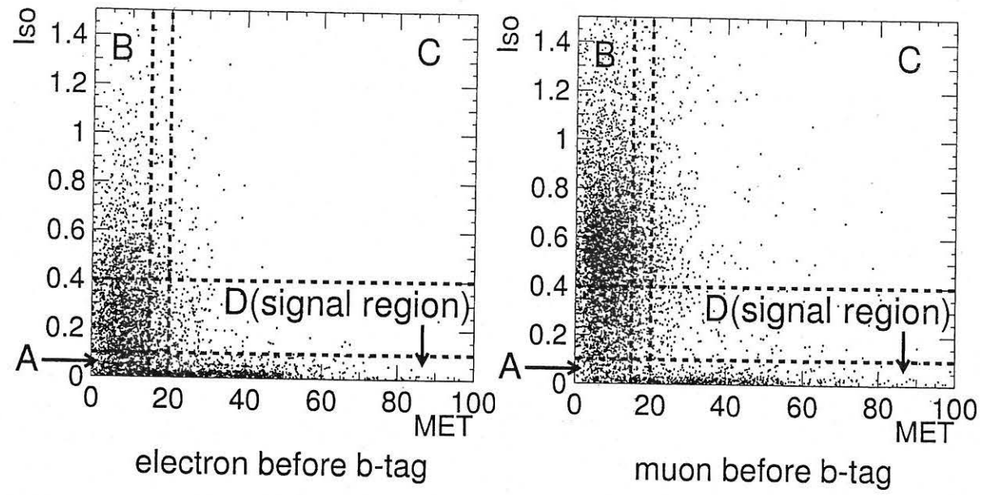

Figure 5.1: Isolation (ISO) vs. missing E_T (MET) distribution of the CDF data with the W+2jet selection except the missing E_T cut and the Isolation cut.

sample	N_A	N_B	N_C	N_D	F_{QCD}
electron	677	667	70	905	7.74%
muon	380	4150	459	706	5.95%
Waited Average					6.96%

Table 5.2: Summary of QCD background calculation in the W+2jet events before SVX b-tag.

5.2 WW, WZ, and $Z \to \tau\tau$ Background

Diboson production can be the background of $Wb\bar{b}$ events. For example, in WZ production case, the W boson decays leptonically and the Z boson decays to $b\bar{b}$. This has a similar final state as the TC signature we search for. The $Z \to \tau\tau$ event can also appear as a background because a lepton and neutrinos from one τ decay can simulates W and the other τ may be tagged to be B hadron because of long life time of τ, 0.3μs ($c\tau = 90\mu$m). Since we know the production cross section of these processes,

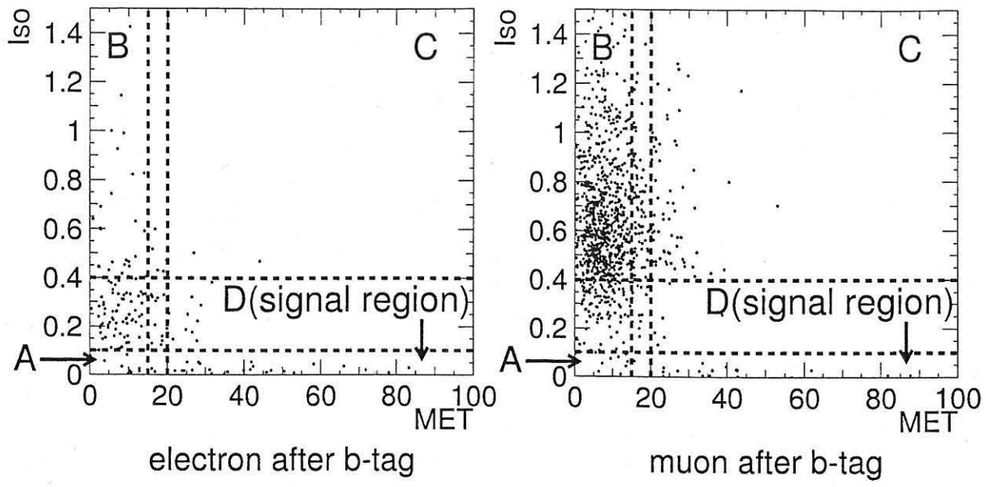

Figure 5.2: Isolation (ISO) vs. missing E_T (MET) distribution of the CDF data with the W+2jet with b-tag selection except the missing E_T cut and the Isolation cut.

sample	N_A	N_B	N_C	N_D	F_{QCD}
electron	11	28	3	24	4.91%
muon	10	747	72	18	5.36%
Waited Average					5.10%

Table 5.3: Summary of QCD background calculation in the W+2jet events after SVX b-tag.

the expected number of the diboson background events are calculated using following equation:

$$N_{expect} = \sigma \cdot \epsilon \cdot \int \mathcal{L}\, dt \tag{5.2}$$

where, σ is the production cross section in $p\bar{p}$ collisions at $\sqrt{s}$ =1.8 TeV , ϵ is the detection efficiency, and $\int \mathcal{L}\, dt$ is the integrated luminosity, 109±7 pb^{-1}. The efficiency is calculated using PYTHIA Monte Carlo generator and the CDF detector simulation. The expected number of fake events from the diboson and $Z \rightarrow \tau\tau$ background is

	N_{QCD} $(109pb^{-1})$
Before b-tag	112.1±8.5
After b-tag	2.1±0.9

Table 5.4: Expected number of events from QCD background for before b-tag and after b-tag.

estimated to be 1.5±0.5 events [28].

5.3 $Wb\bar{b}$ and $Wc\bar{c}$ Background

The number of $Wb\bar{b}$ and $Wc\bar{c}$ background events are computed by the simulation. The fractions are obtained using Monte Carlo samples and the estimated detection efficiency of the SVX $b(c)$-quark tagging. The calculation is done using following expression :

$$N_{Wb\bar{b}} = N_{Wjj} \times (F(1b)_{Wb\bar{b}} \times \epsilon(1b)_{b-tag} + F(2b)_{Wb\bar{b}} \times \epsilon(2b)_{b-tag}) \tag{5.3}$$

- $N_{Wb\bar{b}}$: Expected number of $Wb\bar{b}$ background events in the data sample.
- N_{Wjj} : Expected number of the W+2jet events in the data sample.
- $F(1b)_{Wb\bar{b}}$: Estimated fraction of W+2jet events which has exactly one b jet in the final state. The b jet is defined that any jet with E_T >15 GeV using a cone size of $R = 0.4$, and which has a B hadron within a cone size of $R = 0.4$.
- $\epsilon(1b)_{b-tag}$: Estimated efficiency of the single b-quark tagging by the SVX in the W+2jet events which has exactly one b jet.
- $F(2b)_{Wb\bar{b}}$: Estimated fraction of W+2jet events which has exactly two b jets in the final state.
- $\epsilon(2b)_{b-tag}$: Estimated efficiency of the single b-quark tagging by the SVX in the W+2jet events which has exactly two b jets.

For $Wc\bar{c}$ background, a similar method is utilized. Below, we will discuss how we determine the N_{Wjj}, $F(1b,2b)_{Wb\bar{b}}$, and $\epsilon(1b,2b)_{b-tag}$ values. The calculated values are summarized in table 5.6 . The detail of this method is written in [28, 29].

Determination of the N_{Wjj}

The correction factor of $(1 - F_{QCD})$ is introduced to remove the non-W QCD background. Here, the F_{QCD} is the estimated fraction of QCD events fallen in the W+2jet selected sample. The F_{QCD} has been calculated in the previous section. Even after removing the QCD background, Z boson plus QCD jets events fallen in the W+2jet selected sample cannot be ignored. The event fraction $F(Zjj/Wjj)$ of Z+2jet and W+2jet in the candidate of W+2jet selected events is considered. The Z+heavy flavor background will be discussed later. Diboson events contamination is also removed in the calculation. The N_{Wjj} is calculated using following expression:

$$N_{Wjj} = \frac{1}{1+F(Zjj/Wjj)} \times (N_{Wjj}^{DATA} \times (1 - F_{QCD}) - N_{WW,WZ,Z\to\tau\tau}) \qquad (5.4)$$

where N_{Wjj}^{DATA} is observed number of W+2jet events and $N_{WW,WZ,Z\to\tau\tau}$ is the expected number of WW, WZ, and $Z \to \tau\tau$ events. The estimated N_{Wjj} is summarized in table 5.5 .

Determination of the Fraction, $F(1b)_{Wb\bar{b}}$ and $F(2b)_{Wb\bar{b}}$

In $Wb\bar{b}$ background events, the $b\bar{b}$ pair is produced through a gluon splitting. The leading order feynman diagram and an example of higher order diagrams are illustrated in Figure 5.3 and 5.4. The fraction of these events in W+2jet events is computed using HERWIG [32] and VECBOS [33] Monte Carlo generators. The fractions, $F(1b)_{Wb\bar{b}}$ and $F(2b)_{Wb\bar{b}}$, are calculated from the following equations:

$$F(1b)_{Wb\bar{b}} = \frac{N(1b)_{Wb\bar{b}}}{N_{W+2jet}} \qquad (5.5)$$

	Fraction	Number of events
W+jet candidates		1611
QCD	6.96±2.27%	112±37
$WW, WZ, Z \to \tau\tau$	-	52±13
$F(Zjj/Wjj)$	0.0734±0.0224	
N_{Wjj}^{DATA}		1447
N_{Wjj}		1348
N_{Zjj}		99

Table 5.5: Summary of the number of real Wjj events and Zjj events in the CDF data.

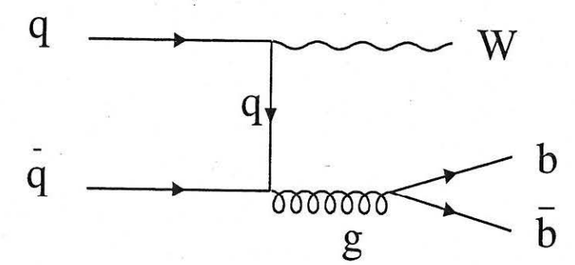

Figure 5.3: Leading order feynman diagram for $Wb\bar{b}$ production.

$$F(2b)_{Wb\bar{b}} = \frac{N(2b)_{Wb\bar{b}}}{N_{W+2jet}} \qquad (5.6)$$

where $N(1b)_{Wb\bar{b}}$ is generated number of $Wb\bar{b}$ events in the Monte Carlo which includes exactly one b jet in the final state, $N(2b)_{Wb\bar{b}}$ is same as the $N(1b)_{Wb\bar{b}}$ but for exactly two b jets in the final state, and N_{W+2jet} is the total generated number of W2jet events in the Monte Carlo. The definition of a b jet is the same as that in the previous section.

Determination of the b tagging efficiency, $\epsilon(1b,2b)_{b-tag}$ and $\epsilon(1b,2b)_{b-tag}$

We calculate the b tagging efficiency separately the events with exactly one b jet and the events with exactly two b jets. The b-tag efficiencies are calculated through the

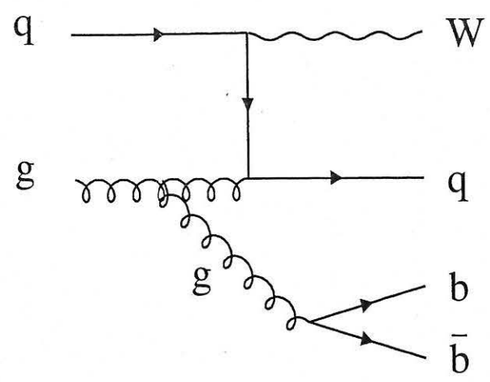

Figure 5.4: An example of the higher order feynman diagram for $Wb\bar{b}$ production.

CDF detector simulation. To correct the slightly optimistic tracking efficiency of the Monte Carlo sample, we apply the scale factor which is evaluated in the study of tracking efficiency on $t\bar{t}$ search analysis[30], and is found to be 0.87±0.07 for b tags and 0.78±0.07 for c tags. This scale factor is applicable for RUN1b only. Since the tagging efficiency for RUN1a sample is slightly worse than RUN1b, we apply another reduction factor of 0.97 to get the estimated tagging rate for the overall 1a+1b sample,

	Fraction	Efficiency	SF $\frac{\epsilon_{1A+1B}}{\epsilon_{1B}}$	$N_{events}(1348)$
1b	$F(1b)_{Wb\bar{b}} = 0.92 \pm 0.03\%$	$22.0 \pm 1.3\%$	0.97	2.65 ± 0.18
2b	$F(2b)_{Wb\bar{b}} = 0.85 \pm 0.25\%$	$38.1 \pm 2.7\%$	0.97	4.23 ± 1.26
1c	$F(1c)_{Wc\bar{c}} = 2.76 \pm 0.07\%$	$4.5 \pm 0.4\%$	0.97	1.62 ± 0.15
2c	$F(2c)_{Wc\bar{c}} = 1.04 \pm 0.27\%$	$8.6 \pm 1.6\%$	0.97	1.17 ± 0.37
Total				9.68 ± 1.33

Table 5.6: Estimated fraction of $Wb\bar{b}$ and $Wc\bar{c}$ event within the selected $W + 2jet$ QCD background and the heavy quark tagging efficiency.

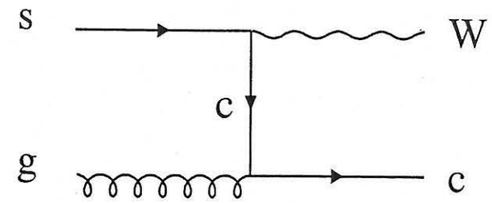

Figure 5.5: The Wc background feynman diagram.

5.4 Wc Background

The Wc background arises through a $Wc\bar{s}$ vertex from the s quark comes from the strange sea quarks in the proton as shown in Figure 5.5 . The expected number of Wc background events are calculated using similar formula as the $Wb\bar{b}$ and $Wc\bar{c}$ background:

$$N_{Wc} = N_{Wjj} \times (1 - F_{QCD}) \times F_{Wc} \times \epsilon(Wc)_{c-tag} \tag{5.7}$$

- N_{Wc} : Expected number of Wc background events in the data sample.
- F_{Wc} : Estimated fraction of Wc events
- $\epsilon(Wc)_{c-tag}$: Estimated efficiency of the SVX heavy quark tagging in the Wc events.

Exactly the same procedure as the $Wb\bar{b}$ and $Wc\bar{c}$ background is used to compute the Wc fraction in the W+2jet sample and the tagging efficiency. Table 5.7 summarizes the calculated Wc fraction, the c-tag efficiency, and the expected number of events applying the charm tagging efficiency scale factor, 0.78±0.07 .

Fraction	Efficiency	SF_{b-tag}	$N_{events}(1348)$
$F_{Wc} = 7.2 \pm 2.2\%$	$6.0 \pm 0.6\%$	0.78±0.07	4.6 ± 1.5

Table 5.7: Estimated fraction of Wc event within the selected $W + 2jet$ QCD background and the c quark tagging efficiency.

5.5 Z and Heavy Flavor Background

The Z boson plus heavy flavor (Z+h.f.) event is one of the background of the W+2jet with b-tag Technicolor signature. If one of the two leptons decayed from Z boson is not identified for some reason, and the missing E_T happens to be large because of the energy measurement fractuation or muon mis-identification, the event can happen to fall into W+2jet with b-tag signature. The Z+h.f. background is computed using similar method as the W plus heavy flavor background. Following sources contribute Z+h.f. background.

- $Zb\bar{b}$ events from gluon splitting similar to Figure 5.3 and 5.4
- $Zc\bar{c}$ events from gluon splitting similar to Figure 5.3 and 5.4
- Events with a $Zb\bar{b}$ vertex originating from gluon splitting shown in Figure 5.6
- Events with a $Zc\bar{c}$ vertex similar to the Wc background shown in Figure 5.7

From the Monte Carlo samples, the Z+h.f. fraction in the W+2jet sample is calculated for each processes [28]. The scale factors for heavy quark tagging are applied to the heavy quark tagging efficiency. We used same scale factor values as the W plus heavy flavor background. Using the expected number of general Z+2jet events in our W+2jet selected sample listed in table 5.5 and the weighted efficiency of all $Z+h.f.$ component, the total number of $Z + h.f.$ background is estimated to be 1.4±0.5 .

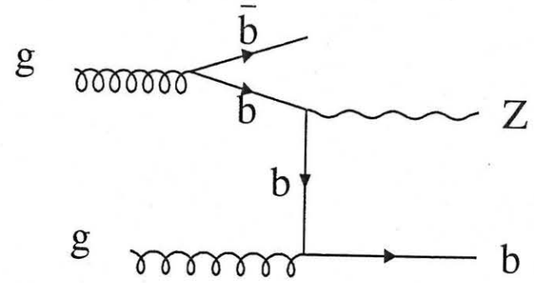

Figure 5.6: The $gg \to Zb\bar{b}$ background feynman diagram.

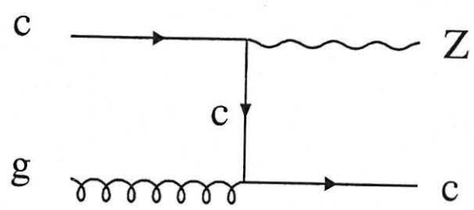

Figure 5.7: The Zc background feynman diagram.

5.6 $t\bar{t}$ Background

The similar method to eliminate the diboson background is used to calculate the $t\bar{t}$ background. The feynman diagram of the $t\bar{t}$ production is shown in Figure 3.1. We assume that the $t\bar{t}$ production cross section is $7.5^{+1.9}_{-1.6}$ pb, which was measured in the CDF experiment [34]. The HERWIG Monte Carlo generator [32] is used to produce the $t\bar{t}$ event in $p\bar{p}$ collisions. The expected number of $t\bar{t}$ background is summarized in Table 5.8.

σ	Efficiency	$N^{109pb}_{expecte}$
7.5 pb	3.6%	5.1±1.9

Table 5.8: Expected number of $t\bar{t}$ background events.

5.7 Single Top Background

Although single top quark productions have not been observed directly, these must appear in $p\bar{p}$ collisions from the Standard Model prediction.[1] Single top is produced through two channels, W-gluon fusion and W^*, having the production cross section of 1.44 pb and 0.74 pb respectively at the CDF experiment [35]. The W-gluon fusion process appears as the W+2jet final state including one b quark in the 2jet as shown in Figure 5.8 . The b quark from a gluon splitting without scattering to the W boson obtains small transverse momentum, and the jet doesn't appear in the central detector region. The W^* process appears as the W+2jet final state including two b quark as shown in Figure 5.9 . We use HERWIG Monte Carlo generator to calculate the detection efficiency of each single top process separately. The expected number of both of the events in our b-tagged data sample is estimated to be 2.4±0.8 .

5.8 Mistag Background

The expected number of b-quark mistag background is calculated using W+2jet pre-tagged data sample. The fake tagging probability is calculated for each jet depending on the jet E_T and number of tracks in the jet taking into account the secondary vertex measurement resolution. The fake event probability by mistagging, P^{event}_{fake}, in W+ 2 jet event is described as follows:

$$P^{event}_{fake} = P^{jet1}_{fake} + P^{jet2}_{fake} - P^{jet1}_{fake} \cdot P^{jet2}_{fake}. \quad (5.8$$

[1]The W+2jet with b-tag signature is a good signature for the single top quark production search This analysis is undergo by T.Kikuchi et.al. using CDF data [31].

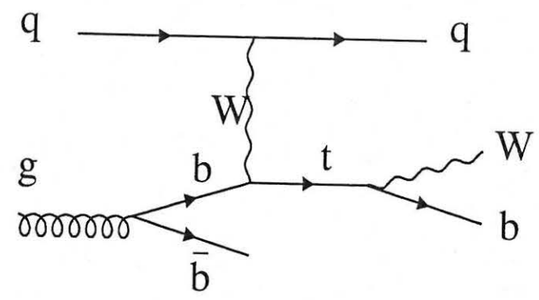

Figure 5.8: Single top quark production feynman diagram in the W-gluon fusion channel.

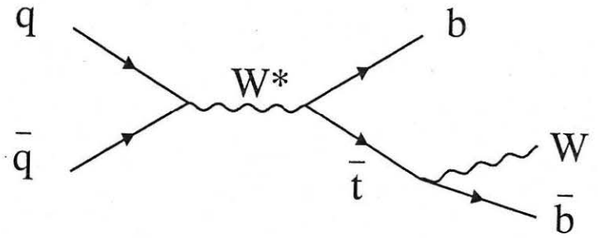

Figure 5.9: Single top quark production feynman diagram in the W^* channel.

By accumulating the P^{event}_{fake} in all the un-tagged W+ 2 jet selected data events, the expected number of the b-quark mistag background is estimated to be 5.1±2.0 .

Chapter 6

Invariant Mass Distributions

In this chapter, we show the reconstruction of the invariant mass , M(jj), of the b-tagged two jets system and the invariant mass , M(Wjj), of the W and b-tagged two jets system. We search for a technipion mass resonance in the M(jj) distribution and a technirho mass resonance in the M(Wjj) distribution. These technicolor particles are expected to have narrow mass resonance states. The mass width is estimated to be at most around 1 GeV/c^2 [14]. Hence, if technicolor particles exist, sharp mass peaks would simultaneously appear in these mass distributions.

6.1 Jet Energy Correction

The jet energy measured may deviate from true value due to a variety of effects These include effects due to (i) calorimeter nonlinearities, (ii) large angle incidenc of low-momentum charged particles to the calorimeter caused by the CDF magneti field, (iii) low calorimeter sensitivity at boundaries between modules and calorimete subsystems, (iv) contributions from events of another $p\bar{p}$ collisions in the same bunc crossing, (v) energy losses from the particles went out of the cone, and (vi) undetecte energy carried by muons or neutrinos. A correction factor is applied to reproduce th average jet E_T correctly and it depends on the jet E_T and the $|\eta|$.

The correction factors increase with jet energies by about 30% typically, and a

described in the Reference [15] and [16]. All mass plots shown as follows are corrected by the jet energy correction factors.

6.2 Neutrino Momentum Estimation

In order to reconstruct the W and two jets mass, we need the values of four momentum of the lepton, the neutrino, and the jets. Since neutrinos rarely interact in the detector, we evaluate the neutrino transverse momentum using the missing transverse energy, $\not\!\!E_T$ information. Here, we still miss the P_z information of the neutrino, P_z^ν . We use the W mass constraint in a lepton-neutrino system to obtain the P_z^ν value. The W mass is expressed as:

$$(M^W)^2 = (E^e + E^\nu)^2 - (P_x^e + P_x^\nu)^2 - (P_y^e + P_y^\nu)^2 - (P_z^e + P_z^\nu)^2$$
$$(\ E^\nu = \sqrt{(P_x^\nu)^2 + (P_y^\nu)^2 + (P_z^\nu)^2} \ ) \ . \tag{6.1}$$

Here, since all variables are measured by the CDF detector except the P_z^ν, the P_z^ν value is obtained analytically and the solution is simply expressed as:

$$P_z^\nu = \alpha \pm \sqrt{\beta} \ , \tag{6.2}$$

where the α or the β is a real value. We use the 80.3 GeV/c^2 as the W boson mass. If the β is greater than zero, we take the smaller $|P_z^\nu|$ from the two solutions. If the β is smaller than zero, which is no real solution case, we take the real part of the solution, that is, α. The 'no real solution' result can be obtained if the lepton or neutrino energy is mis-measured,

Figure 6.1 shows the results of the study of the method described above. On the left side of Figure 6.1, the P_z^ν information of the generator level (GENP) output of the PYTHIA Monte Carlo generator and the three kinds of solutions after running the offline analysis code. We compare between the P_z^ν in the GENP and the P_z^ν of

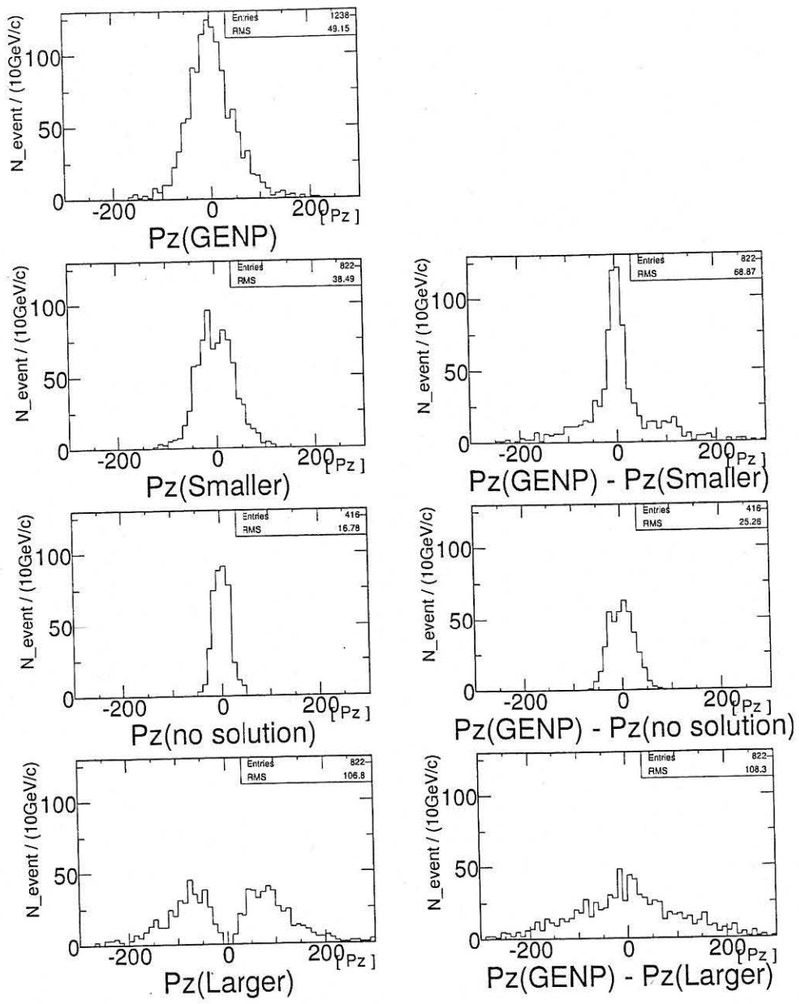

Figure 6.1: The $|P_z^\nu|$ distributions from Monte Carlo generator level (GENP) (left top) and from three kind of solutions after offline analysis (left other three). In the plots, 'no solution' represents the real part of the solution in the no real solution case. Right plots show the difference between the P_z^ν in GENP and the $|P_z^\nu|$ of the each of three solutions. Technicolor events of PYTHIA v6.1 Monte Carlo generator are used. The Technicolor particles masses are assumed to be $M(\pi_T)$=90 GeV/c^2 and $M(\rho_T)$=180 GeV/c^2 .

each solution after offline analysis. These distributions are shown on the right side of Figure 6.1. When we get the correct P_z^ν, the difference should be small. The solutions of the smaller $|P_z^\nu|$ and real part value in the 'no real solution' events show a narrow peak around zero, while the solution of larger $|P_z^\nu|$ has much broader distribution than the others. Technicolor events of PYTHIA v6.1 Monte Carlo generator are used with technicolor particles masses, $M(\pi_T)$=90 GeV/c^2 and $M(\rho_T)$=180 GeV/c^2 . By looking at the generator level information only, we find that the smaller $|P_z^\nu|$ is the correct solution $\sim$ 60%, the larger $|P_z^\nu|$ solution is correct $\sim$ 30%, and there is no real solution $\sim$ 10% of the times.

6.3 Mass Distributions

Figure 6.2 shows the invariant mass of the dijet system and the $W+$ 2 jet system. The CDF data are presented by solid circles. The shaded area indicates the background expected from all known channels for the integrated luminosity of 109 pb^{-1}. The dashed line shows the signal expected with the mass combination of $M(\pi_T)$=90 GeV/c^2 and $M(\rho_T)$=180 GeV/c^2 . Number of events for signal and background simulated are normalized to the expected number of events for 109 pb^{-1}. Although a slight excess of the number of events in the CDF data is seen, there is no apparent mass peak in both of the distributions. The excess of number of events in the CDF data is $1.5\times\sigma$ taking into account the statistical and the systematic uncertainty of the background estimation. The standard deviation, σ, is obtained using following calculation.

$$\sigma = \sqrt{(\sqrt{31.6})^2 + 4.3^2} = 7.1 \tag{6.3}$$

where the $\sqrt{31.6}$ is the statistical uncertainty of the expected number of background and the 4.3 is the systematic uncertainty of the background estimation as shown in Table 5.1.

Figure 6.3 shows the two dimensional plot of M(jj) vs. M(Wjj). The background events are presented by small dots and the CDF data are shown as solid circles. The background shown is corresponding to the integrated luminosity of 22 fb^{-1}. Technicolor events is expected to make a narrow cluster on this mass plot if technicolor particle exists. The CDF data is in good agreement with the expected background distribution.

In order to get higher signal to noise ratio for this technicolor search, we will apply further selection cuts in the next Chapter. Until this Chapter, the selection cuts are the same for any technicolor mass combinations. In the next Chapter, we will apply different optimum selection cuts for the different technicolor particles mass combinations.

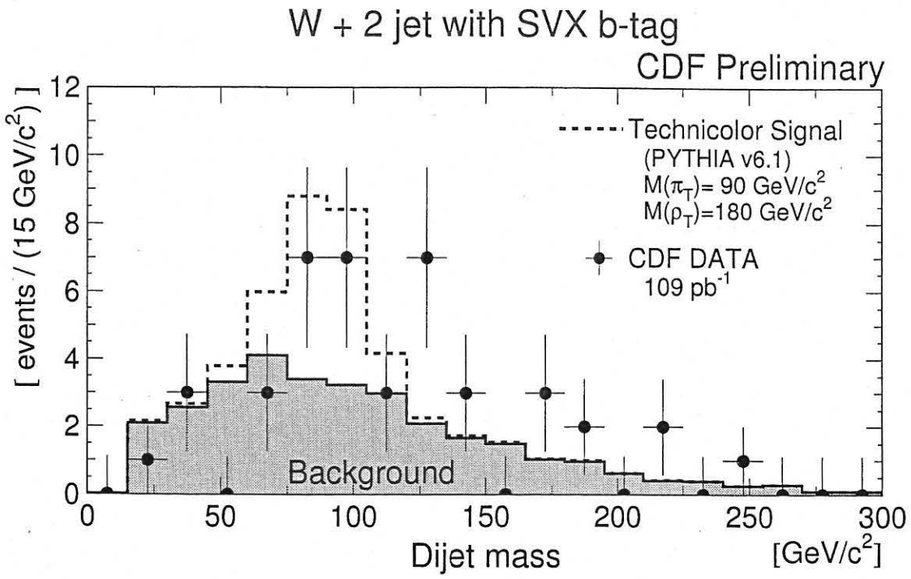

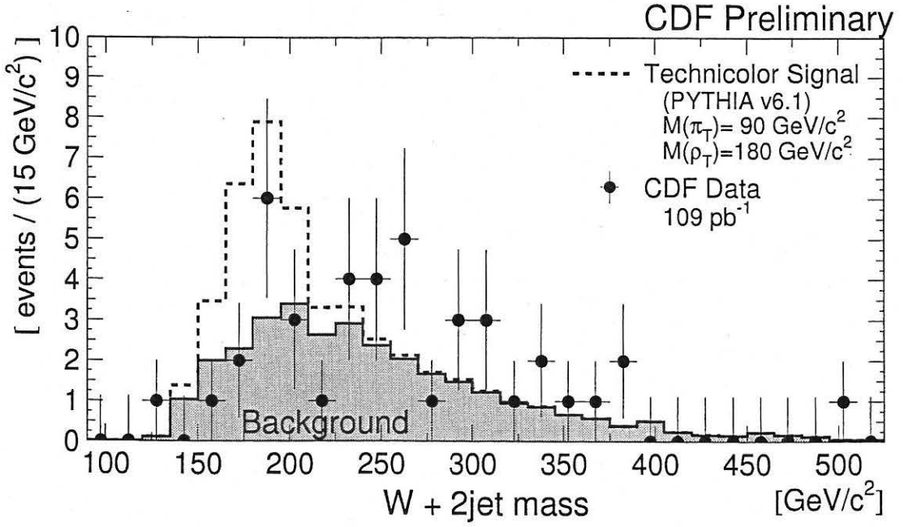

Figure 6.2: The invariant mass distribution of the dijet system and W+ 2 jet system for the b-tagged W+ 2 jet data sample. Filled area shows expected background distribution. The background distribution is the weighted sum of all the expected background sources. Dashed line shows the expected Technicolor signal distribution added to the background distribution. The mass combination is assumed to be M(π_T)=90 GeV/c^2 and M(ρ_T)=180 GeV/c^2 . Number of events for signal and background are normalized to the expected number of events for 109 pb^{-1}. Dots show CDF data.

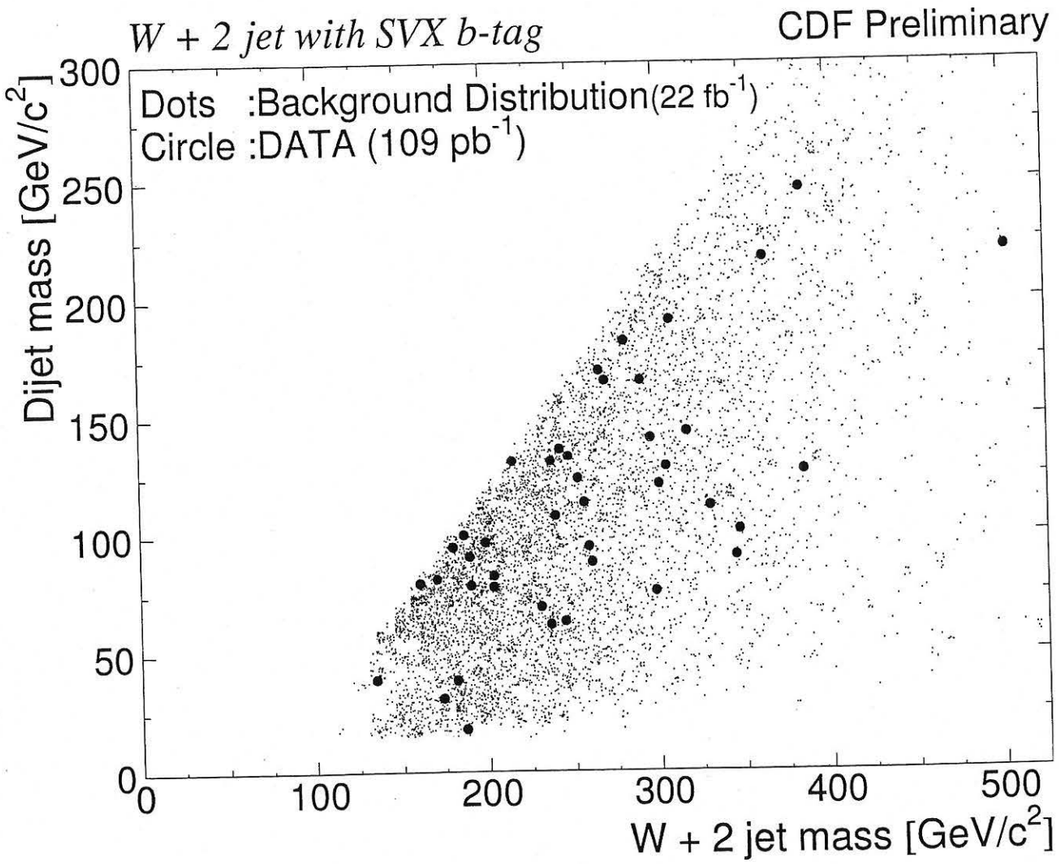

Figure 6.3: The invariant mass of the dijet system vs. $W+$ 2 jet system for the $W+$ 2 jet sample with b-tag. The data and the background distribution are shown. The background distribution is the weighted sum of all the expected background sources.

Chapter 7

Mass Dependent Selection Cuts

In this chapter, we discuss further selection cuts in addition to the W+2jet with b-tag selection to improve the signal to noise ratio of the data. The first cuts are the topology cuts which are applied to the ϕ opening angle between two jets, $\Delta\phi(jj)$, and the P_T of the dijet system, $P_T(jj)$ [14]. After passing through the topology cuts, mass window cuts are placed on the dijet mass distribution and the W+2jet mass distribution. The individual topology and mass window cuts are optimized to each mass combination by using Monte Carlo simulation. Forty-seven different optimum cut values are set for the mass combinations described in Chapter 4. Finally these cuts are applied to the real data.

7.1 Topology Cuts

7.1.1 Topology Cuts

We search for the single technirho production of the quark and anti-quark annihilation in $p\bar{p}$ collisions as shown in Figure 1.2. In this production mode, the P_T of the technirho is small because the P_T of the initial quarks are small. Since the technicolor particles are searched in the characteristic mass region of $\mathrm{M}(\pi_T) + \mathrm{M}(W) \simeq \mathrm{M}(\rho_T)$, technipions are produced with small P_T. Consequently the opening angle ϕ between two jets, $\Delta\phi(jj)$, is expected to be around 180° whereas the background has flatter distribution.

The transverse momentum of the two jets system, $P_T(jj)$, which corresponds to the technipion P_T, is expected to have a peak around zero whereas the background has broader distribution.

Figure 7.1 shows the $\Delta\phi(jj)$ and the $P_T(jj)$ distributions with the corresponding sensitivity distributions for the mass combination of $M(\pi_T) = 90$ GeV/c^2 and $M(\rho_T) = 173$ GeV/c^2 . The sensitivity is defined as '$S/\sqrt{B}$', where the S is the expected number of signal events and the B is the expected number of background events. The left top plot in Figure 7.1 shows the $\Delta\phi(jj)$ distributions of the TC signal and the background for the $W+$ 2 jet with b-tag selection. Number of events are normalized to the expected number of events for 109 pb^{-1}. Most of the technicolor signa events distributs greater than 2.0 radian on the $\Delta\phi(jj)$ plot and the signal distribution is clearly different from the flatter background distribution. We can reduce th background events without loosing the signal efficiently by imposing the $\Delta\phi(jj)$ cut The optimum cut value is shown as a dashed vartical line. The left bottom plot show the similar plot for the $P_T(jj)$ distribution. This is also effective cut to improve th $S/\sqrt{B}$ ratio.

7.1.2 Mass Dependence of the Topology Cuts

The two more examples plots are shown in Figure 7.2 [$M(\pi_T)$=90GeV/c^2 , $M(\rho_T)$=180 and Figure 7.3 [$M(\pi_T)$=90 GeV/c^2 , $M(\rho_T)$=190 GeV/c^2]. From Figure 7.1 to Fi ure 7.3, the technipion mass is fixed to be 90 GeV/c^2 . The $\Delta\phi(jj)$ and $P_T(jj)$ of tl technicolor signal have broader distributions for the higher technirho mass, becau the larger technirho mass gives higher Q value and more momentum to the technipic For this reason, if the technirho mass gets larger for the same technipion mass, t topology cuts get looser.

7.1.3 Optimum Cut Values

The optimum values of the topology cuts are set as the cut values which have the maximum value of the $S/\sqrt{B}$. We apply the topological cuts on the two dimentional plane of the $\Delta\phi(jj)$ and the $P_T(jj)$ to attain the maximum $S/\sqrt{B}$ as shown in Figure 7.4. At the mass combination of $M(\pi_T) = 90$ GeV/c^2 and $M(\rho_T) = 180$ GeV/c^2 , the highest $S/\sqrt{B}$ is given at the cut value combination of $\Delta\phi(jj) = 2.1$ and $P_T(jj) = 40$ GeV/c . By applying these topology cuts, background retains only 27.7 % while the signal efficiency is 83.5 %. The $S/\sqrt{B}$ is improved from 2.6 to 4.1 . Table 7.1 summarizes the cut values, signal efficiency, the background retain, and the $S/\sqrt{B}$ before and after topology cuts for the various mass combinations.

7.1.4 Mass Distribution of Real Data Selected

The signal distribution expected and the optimum cut values are shown in Figure 7.5-a. As shown in the right plot of Figure 7.5-a, the topology cuts on the $\Delta\phi(jj)$ and the $P_T(jj)$ are applied to the real data.

Figure 7.6 shows the $M(jj)$ and the $M(Wjj)$ distributions of the data together with the simulated technicolor signal and background. The solid dots are the CDF data selected. The solid line shows background. The dashed line shows the simulated signal. The CDF data agrees well to the background expected from the Standard Model for both $M(\pi_T)$ and $M(\rho_T)$.

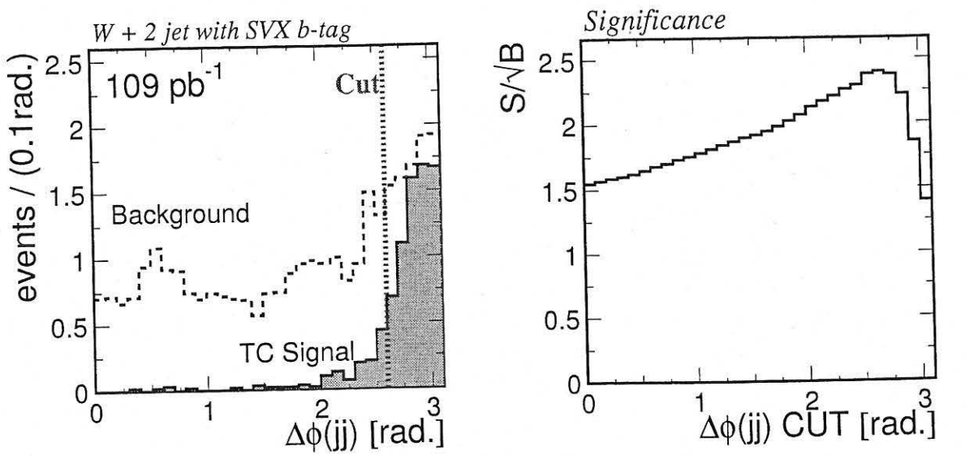

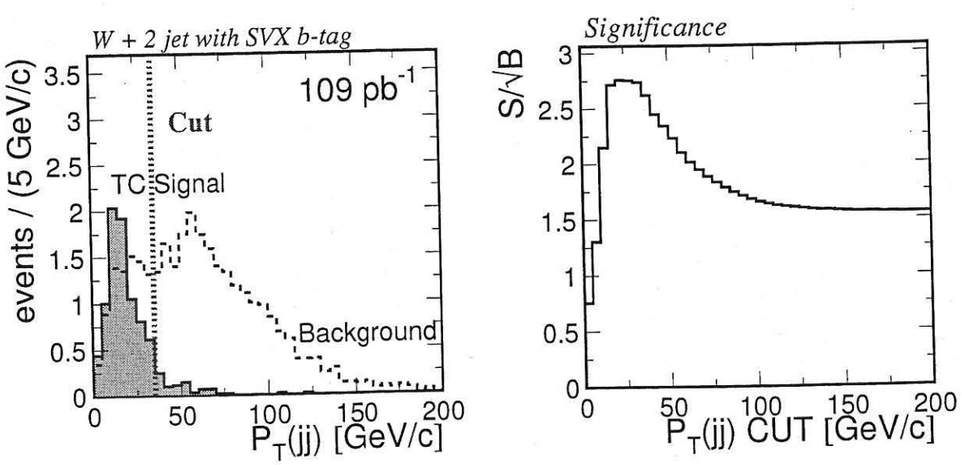

Figure 7.1: The $\Delta\phi(jj)$ and the $P_T(jj)$ distributions of the TC signal and the background for the $W+$ 2 jet with b-tag selection. The signal distributions expected and the optimum cut values at $M(\pi_T)$=90 GeV/c^2 and $M(\rho_T)$=173 GeV/c^2 mass combination are shown. Number of events are normalized to the expected number of events for 109 pb^{-1}. Right plots show the $S/\sqrt{B}$ of the independent cut of the $\Delta\phi(jj)$ cut or the $P_T(jj)$ cut as a function of the each cut value.

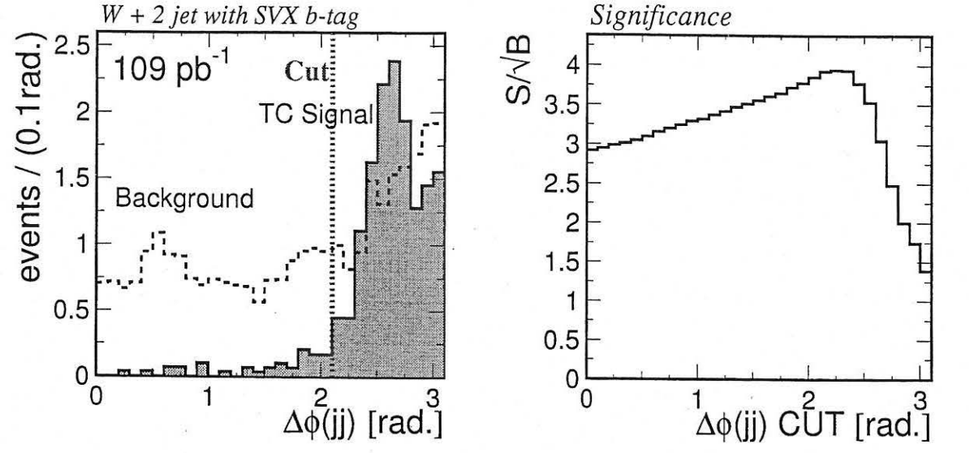

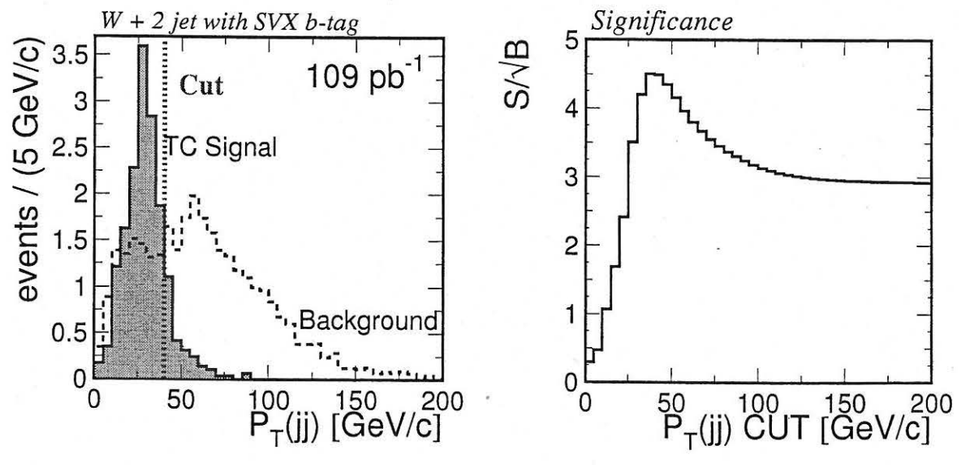

Figure 7.2: The $\Delta\phi(jj)$ and the $P_T(jj)$ distributions of the TC signal and the background for the $W+$ 2 jet with b-tag selection. The signal distributions expected and the optimum cut values at $M(\pi_T)$=90 GeV/c^2 and $M(\rho_T)$=180 GeV/c^2 mass combination are shown. Number of events are normalized to the expected number of events for 109 pb^{-1}. Right plots show the $S/\sqrt{B}$ of the independent cut of the $\Delta\phi(jj)$ cut or the $P_T(jj)$ cut as a function of the each cut value.

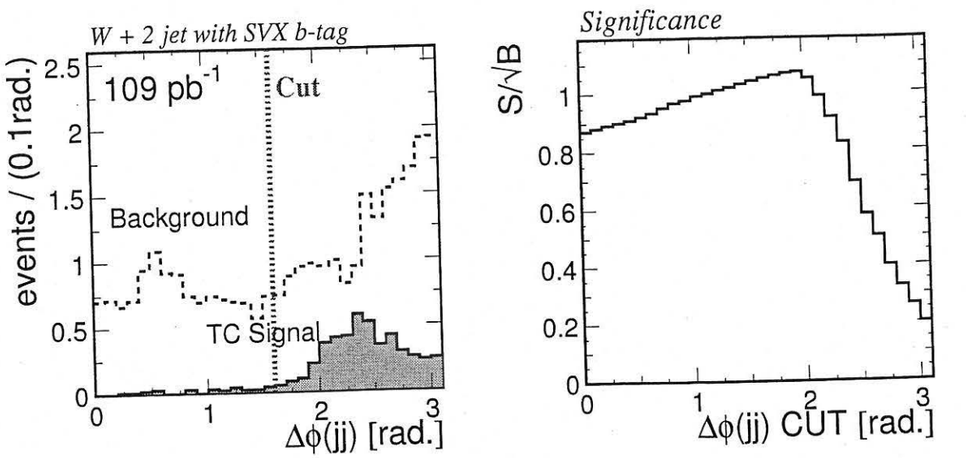

Figure 7.3: The $\Delta\phi(jj)$ and the $P_T(jj)$ distributions of the TC signal and the bac ground for the $W+$ 2 jet with b-tag selection. The signal distributions expected ar the optimum cut values at M(π_T)=90 GeV/c^2 and M(ρ_T)=190 GeV/c^2 mass combin tion are shown. Number of events are normalized to the expected number of even for 109 pb^{-1}. Right plots show the $S/\sqrt{B}$ of the independent cut of the $\Delta\phi(jj)$ cut the $P_T(jj)$ cut as a function of the each cut value.

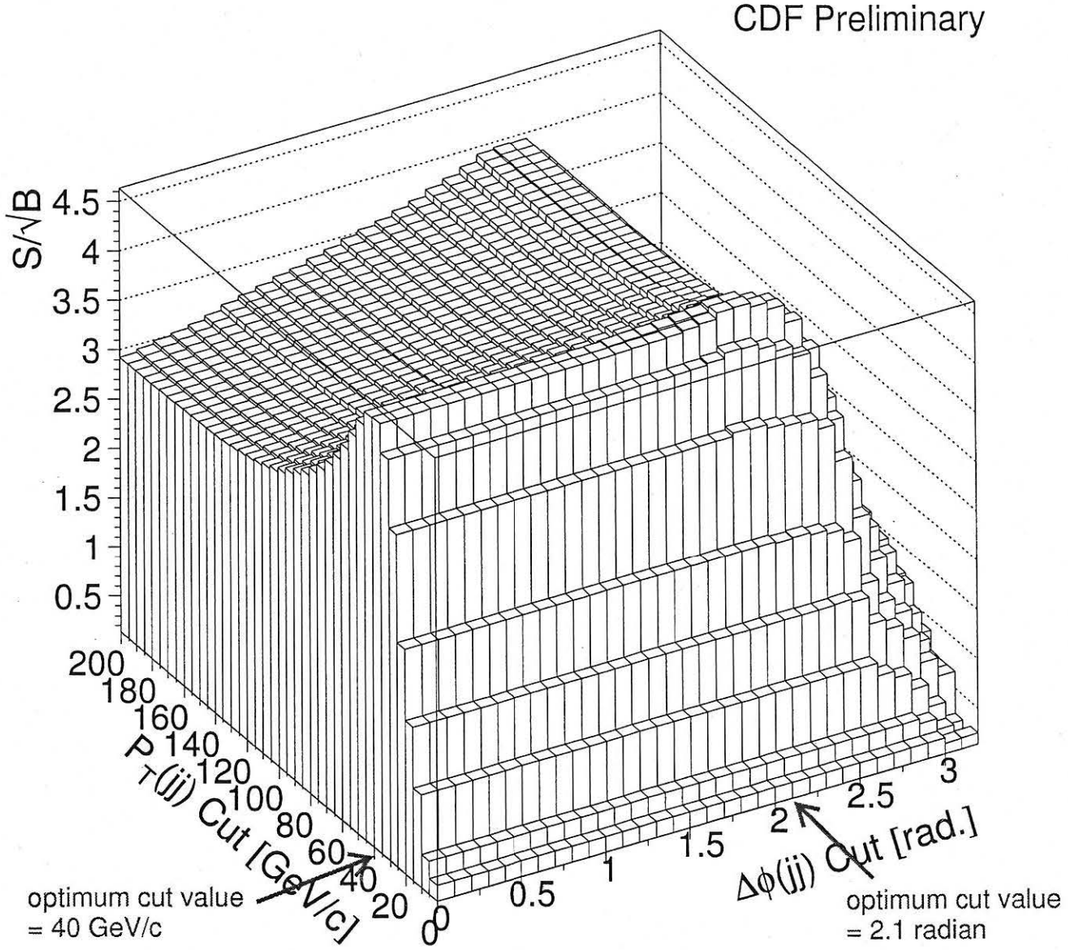

Figure 7.4: S/$\sqrt{B}$ distribution as functions of the $\Delta\phi(jj)$ cut value and the $P_T(jj)$ cut value. We select each cut values at the highest tower as optimum cut values.

CDF Preliminary

M_{π_T}, M_{ρ_T}	Cut Value $\delta\phi$[rad],p_T[GeV/c]	Eff/B.G.Retain	$S/\sqrt{B}$ before Cuts		$S/\sqrt{B}$ after Cuts
80,165	2.2, 30	84.0 % / 21.3 %	0.5	→	1.0
80,170	2.0, 40	85.4 % / 28.2 %	0.6	→	0.9
80,180	1.5, 55	86.2 % / 41.9 %	0.4	→	0.5
85,170	2.5, 30	78.8 % / 18.8 %	2.4	→	4.3
85,175	2.1, 40	83.0 % / 27.7 %	1.0	→	1.6
85,180	1.9, 50	87.1 % / 35.9 %	0.7	→	1.0
90,175	2.5, 35	80.3 % / 21.2 %	2.1	→	3.7
90,180	2.1, 40	83.5 % / 27.7 %	2.6	→	4.1
90,185	2.0, 55	87.4 % / 37.3 %	1.3	→	1.8
95,180	2.3, 40	89.3 % / 26.4 %	2.0	→	3.4
95,185	2.0, 45	88.6 % / 32.1 %	2.6	→	4.1
95,190	1.9, 50	90.1 % / 35.9 %	2.3	→	3.4
100,190	2.0, 40	85.3 % / 28.2 %	2.3	→	3.7
100,195	2.1, 55	87.9 % / 36.0 %	2.1	→	3.1
100,200	1.8, 65	91.5 % / 45.7 %	1.8	→	2.4
105,195	2.2, 45	87.9 % / 30.7 %	2.0	→	3.2
105,200	2.1, 55	87.7 % / 36.0 %	2.0	→	2.9
105,205	1.9, 60	90.1 % / 41.6 %	1.6	→	2.3
110,200	2.1, 50	91.2 % / 33.7 %	1.7	→	2.7
110,205	2.0, 55	89.1 % / 37.3 %	1.8	→	2.6
110,210	1.9, 65	92.0 % / 43.8 %	1.5	→	2.1
115,205	2.2, 55	93.5 % / 34.8 %	1.6	→	2.5
115,210	2.0, 55	89.1 % / 37.3 %	1.6	→	2.3
115,215	2.1, 65	89.3 % / 40.1 %	1.4	→	2.0

Table 7.1: The optimum topology cuts values, signal efficiency and background retair of the topology cuts, and the S/$\sqrt{B}$ before and after topology cuts.

CDF Preliminary

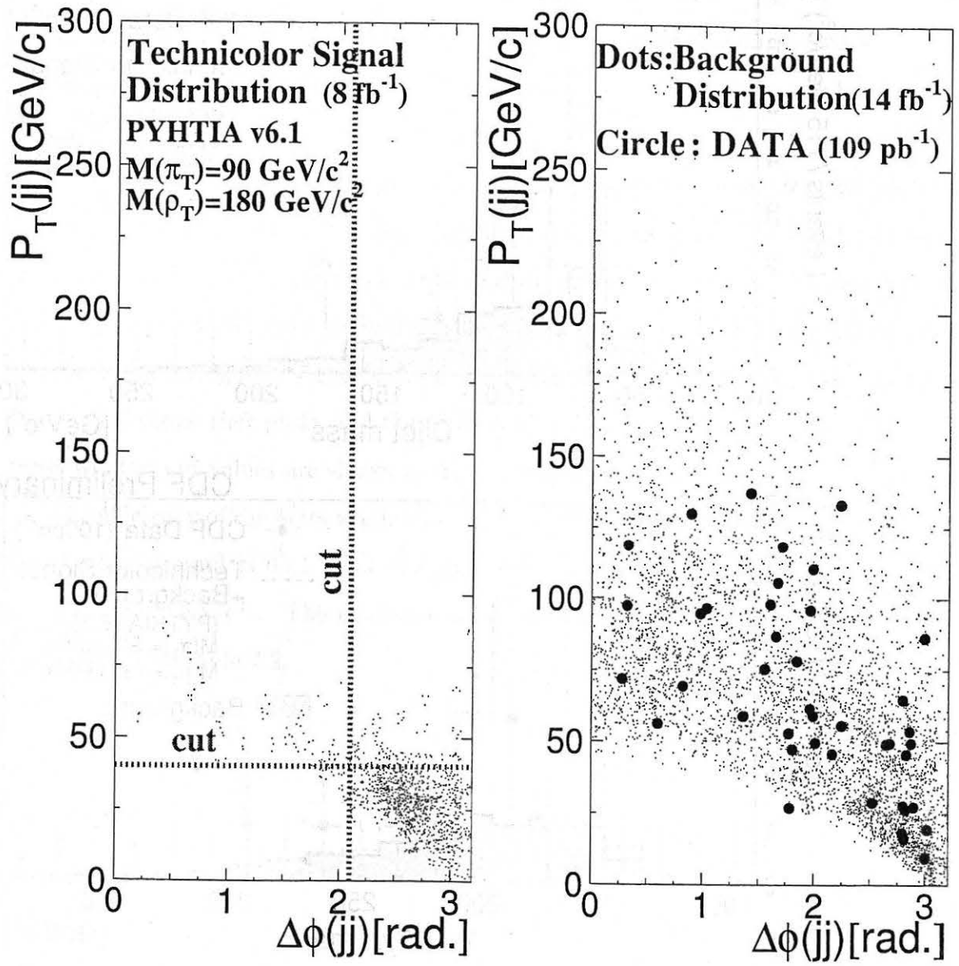

Figure 7.5: The $P_T(jj)$ vs. $\Delta\phi(jj)$ distribution of the TC signal (left plot), the data and the background (right plot) in b-tagged $W+$ 2 jet data sample. The TC mass combination is M(π_T)=90 GeV/c^2 and M(ρ_T)=180 GeV/c^2 . The optimum cut values at this mass combination are shown in the left plot.

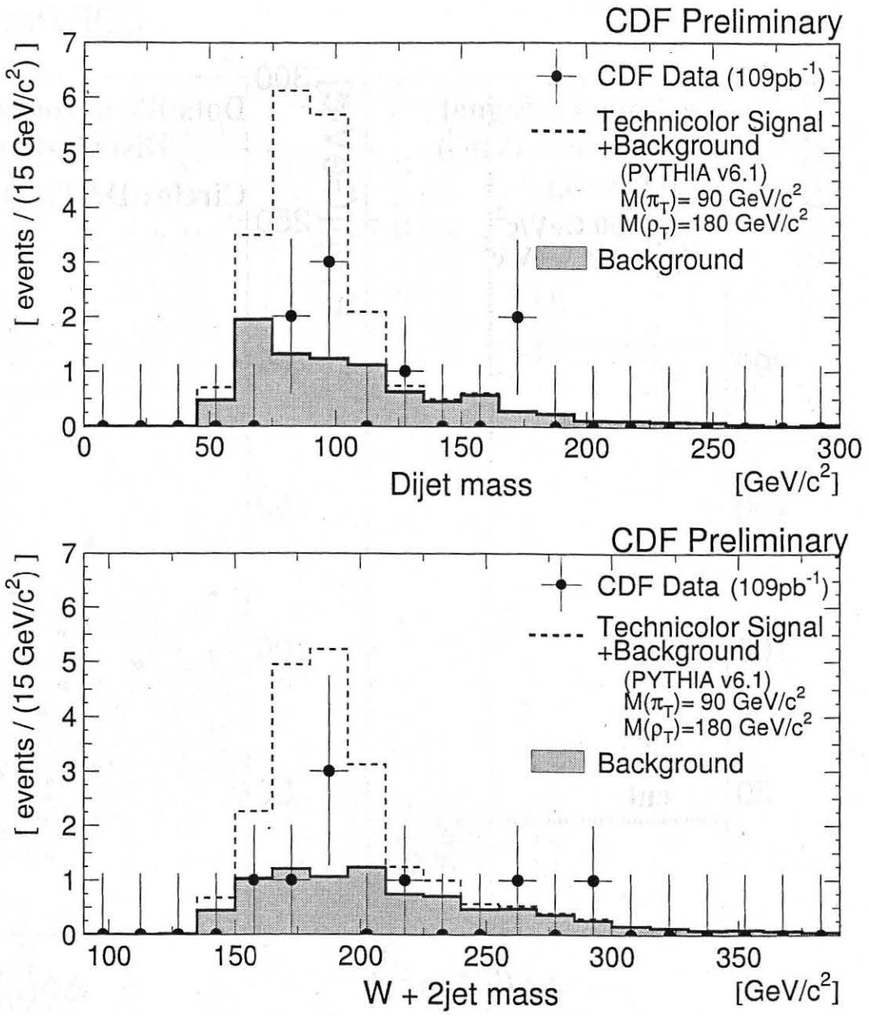

Figure 7.6: The invariant mass distribution of the dijet system and $W+$ 2 jet syste for the b-tagged $W+$ 2 jet data sample after topology cuts. Filled area shows expecte background distribution. The background distribution is the weighted sum of all tl expected background sources. Dashed line shows the expected Technicolor signal di tribution added to the background distribution. The mass combination is assume to be M(π_T)=90 GeV/c^2 and M(ρ_T)=180 GeV/c^2 . Number of events for signal ar background are normalized to the expected number of events for 109 pb^{-1}. Dots shc CDF data.

7.2 Mass Window Cuts

The final criteria to improve the $S/\sqrt{B}$ ratio is to apply the mass window cuts. Figure 7.7 shows an example of the mass window cuts at the mass combination of M(π_T) = 90 GeV/c^2 and M(ρ_T) = 180 GeV/c^2 . The TC signal dijet mass and the $W+$ 2 jet mass distributions are plotted with the background in the top two plots of Figure 7.7. We fit the M(jj) and M(Wjj) distributions of the TC signal with Gaussian distribution to compute the mean value and the standard deviation (σ). We require that M(jj) and M(Wjj) to be within $\pm$ 3$\times\sigma$ from the mean values of the fitting. The bottom plots in Figure 7.7 shows the two dimensional plot of the M(jj) vs. M(Wjj) for the TC signal (left plot), and the CDF data and the background (right plot). The mass window cut values are shown as dashed lines on the plots.

The efficiency of the mass window cuts for the TC signal is 97.0 % and the efficiency for the background is 65.1 % at the mass combination of M(π_T) = 90 GeV/c^2 and M(ρ_T) = 180 GeV/c^2 . The efficiency values for the various mass combinations are summarized in Table 7.2.

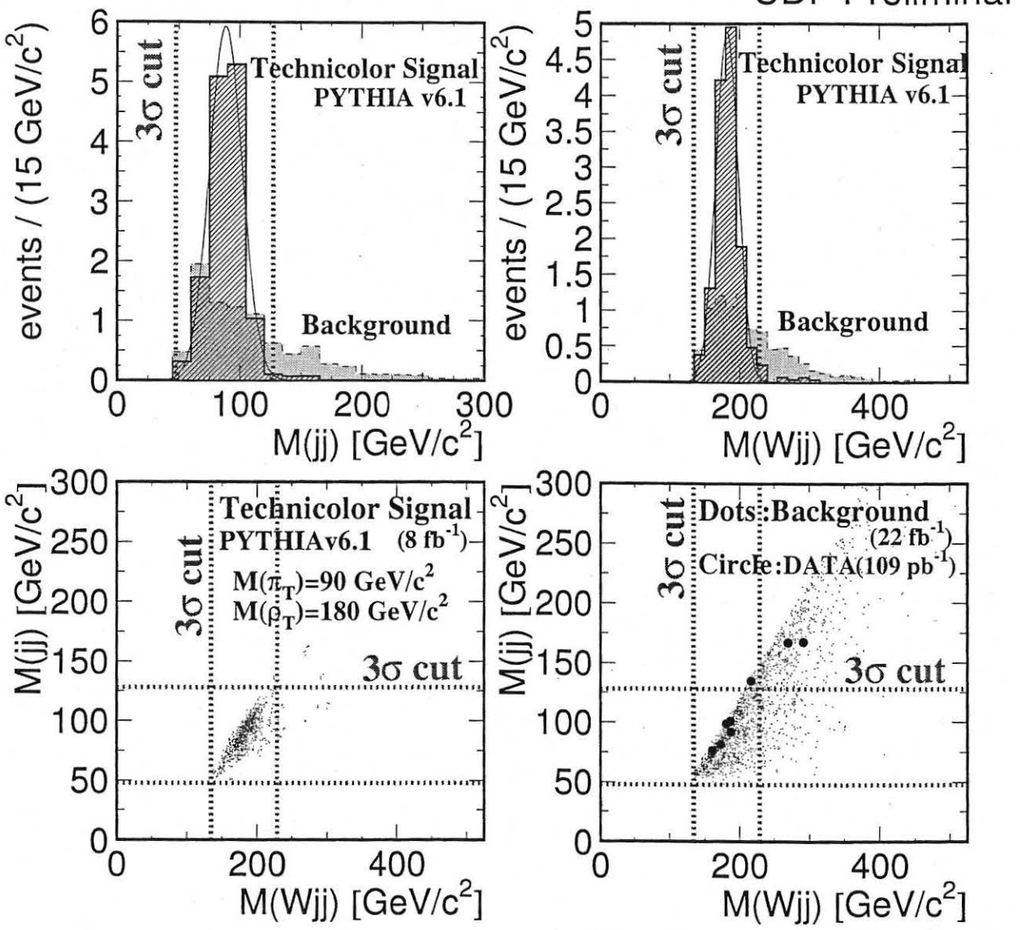

Figure 7.7: The dijet mass and the $W+$ 2 jet mass of the TC signal, background, and data after topology cuts at M(π_T)=90 GeV/c^2 and M(ρ_T)=180 GeV/c^2 mass combination are shown. After the topology cuts, we applied mass window cuts for the M(jj) and the M(Wjj). The cut values are 3σ of the Gaussian fitting of the technicolo Monte Carlo.

CDF Preliminary

M(π_T),M(ρ_T)	Efficiency	B.G. retain
80,165	96.7 %	60.9 %
80,170	96.1 %	60.6 %
80,180	96.1 %	57.4 %
85,170	95.3 %	64.0 %
85,175	96.5 %	62.8 %
85,180	95.4 %	57.3 %
90,175	97.7 %	62.7 %
90,180	97.0 %	65.1 %
90,185	97.1 %	61.1 %
95,180	97.8 %	67.0 %
95,185	97.6 %	64.1 %
95,190	96.4 %	65.0 %
100,190	97.5 %	70.5 %
100,195	97.0 %	66.2 %
100,200	97.4 %	67.8 %
105,195	97.4 %	68.0 %
105,200	97.4 %	65.0 %
105,205	97.4 %	66.9 %
110,200	98.0 %	70.4 %
110,205	98.7 %	69.6 %
110,210	97.5 %	70.8 %
115,205	98.0 %	74.6 %
115,210	98.7 %	71.3 %
115,215	97.5 %	71.0 %

Table 7.2: The signal efficiency and the background retaining of the mass window cuts after topology cuts for each mass combination.

Chapter 8

Results and Cross Section Limits

We compare between the expected number of background events and the remaining CDF data after applying all selection cuts. The CDF data agrees well with the background expected from the Standard Model at all mass combinations we examined. These numbers are listed in Table 8.1. Since there is no evidence for the Technicolor signal in the CDF data, we set cross section upper limits and finally determine the excluded region in the M(π_T) vs. M(ρ_T) mass plane at the 95% confidence level. The 27% of the systematic uncertainty is taken into account for the cross section upper limits. The method for obtaining the systematic uncertainty and the cross section upper limits are described in this Chapter.

8.1 Systematic Uncertainties

We estimated the following systematic uncertainties on the determination of the efficiency:

- Initial state QCD and QED radiation:

  We turn off the initial state radiation switch in the PYTHIA and calculate the total efficiency. We took the 50 % of the difference as a systematic uncertainty.

- Final state QCD and QED radiation:

CDF Preliminary

M_{π_T}, M_{ρ_T}	$\sigma_{counting}$ $\rho_T^{\pm}\to W+\pi_T^0$ $\rho_T^0\to W+\pi_T^{\pm}$	$N_{Signal}^{allcuts}$ (109 pb^{-1})	$N_{B.G.}^{allcuts}$ (109 pb^{-1})	DATA	95 % C.L. limits $N_{95\,\%limit}$	$\sigma_{95\,\%limit}$
80,165	3.8 pb	2.4	4.1±0.6	5	8.2	12.8 pb
80,170	3.7 pb	2.6	5.4±0.7	5	7.3	10.5 pb
80,180	2.8 pb	1.9	7.6±1.0	9	10.5	15.8 pb
85,170	14.1 pb	10.2	3.8±0.5	5	8.4	11.7 pb
85,175	6.9 pb	4.5	5.5±0.8	5	7.3	11.1 pb
85,180	4.6 pb	3.3	6.5±0.9	7	8.9	12.3 pb
90,175	11.9 pb	9.4	4.2±0.6	5	8.1	10.2 pb
90,180	15.7 pb	11.8	5.7±0.8	5	7.1	9.5 pb
90,185	7.5 pb	6.2	7.2±1.0	7	8.4	10.3 pb
95,180	9.6 pb	9.6	5.6±0.8	6	8.4	8.3 pb
95,185	13.0 pb	12.5	6.4±0.9	6	7.9	8.1 pb
95,190	12.6 pb	11.0	7.5±1.0	8	9.4	10.7 pb
100,190	10.9 pb	10.9	6.5±0.9	6	7.8	7.8 pb
100,195	10.9 pb	9.9	7.1±1.0	8	9.7	10.6 pb
100,200	9.8 pb	9.0	9.7±1.3	14	15.4	16.7 pb
105,195	9.2 pb	9.6	6.6±0.9	6	7.7	7.4 pb
105,200	9.3 pb	9.5	7.4±1.0	8	9.5	9.2 pb
105,205	8.5 pb	8.1	8.8±1.2	12	13.5	14.3 pb
110,200	7.8 pb	8.5	7.5±1.0	8	9.4	8.6 pb
110,205	8.0 pb	8.6	8.2±1.1	10	11.3	10.5 pb
110,210	7.4 pb	7.9	9.8±1.3	13	13.8	13.0 pb
115,205	6.5 pb	8.0	8.2±1.1	8	8.9	7.3 pb
115,210	6.9 pb	7.7	8.4±1.2	10	11.2	10.1 pb
115,215	6.6 pb	6.9	9.0±1.2	10	10.7	10.1 pb

Table 8.1: Production cross section times branching ratio of $\rho_T^{\pm}\to W+\pi_T^0$ and $\rho_T^0\to W+\pi_T^{\pm}$, expected number of signal and background events for 109 pb^{-1}, and remaining data after all cuts are shown. 95 % confidence level upper limits of expected number of signal events over the background and 95 % confidence level upper limits of the production cross sections are listed in the right two columns.

We used the similar method as in the initial state radiation.

- Choice of the parton distribution function:

  We generated Monte Carlo samples using GRVHO and MRSG. We took the maximum difference of the total efficiency from CTEQ4L.

- Jet energy scale:

  We varied the JTC96S jet energy correction, +5 %, -5 % (absolute) and +5 %, -5 % (relative) to the default Monte Carlo sample. We took the maximum total efficiency difference from the standard total efficiency as our systematic uncertainty. Because we use uncorrected jet energy for the 2 jet selection, the jet energy scale variation affects only after topology cuts. If the topology cuts can be selected tightly (the mass combination is near to the kinematical threshold), the jet energy scale variation largely affects on the efficiency. When the topology cuts are selected loosely the effect for the efficiency is smaller.

- lepton ID : 5 %

  Weighted average of the electron and muon trigger efficiency. This has been studied in [36].

- b-tag : 9 %

  The uncertainty has been studied in [36].

- luminosity : 7 %

- Monte Carlo statistics : 5 ~6 %

The systematic uncertainties at four mass combination are shown in Table 8.2 We select the mass combination from the low mass combination edge to the high mass combination edge in our search region. The total systematic uncertainties are estimated as a quadratic sum of all the components to be from 24 % to 27 %. We don't

CDF Preliminary

Source	M(π_T),M(ρ_T) 85,170	M(π_T),M(ρ_T) 90,180	M(π_T),M(ρ_T) 100,200	M(π_T),M(ρ_T) 110,200
Initial state radiation	9 %	10 %	11 %	11 %
Final state radiation	15 %	19 %	17 %	15 %
pdflib	8 %	6 %	4 %	4 %
Jet energy scale	5 %	4 %	1 %	2 %
Trigger	5 %	5 %	5 %	5 %
Lepton ID	5 %	5 %	5 %	5 %
b-tag	9 %	9 %	9 %	9 %
Luminosity	7 %	7 %	7 %	7 %
MC statistics	6 %	6 %	5 %	5 %
TOTAL	25 %	27 %	25 %	24 %

Table 8.2: Systematic Uncertainties at four different mass combination.

see any apparent mass dependence of the total systematic uncertainties in the four mass combinations. Therefore, the value of 27 % is used as a systematic uncertainty for every mass combinations for setting limits.

8.2 Cross Section Limits

Since we don't see any excess of data over the background as shown in Table 8.1, we set cross section limits by following formula:

$$\sigma_{95\,\%\,limit} = \frac{N_{95\,\%\,limit}}{109\,pb^{-1} \cdot \varepsilon_{total} \cdot BR(W \to e\nu, \mu\nu)} \tag{8.1}$$

$$\varepsilon_{total} = \varepsilon_{W+2\,jet\,b\text{-}tag} \cdot \varepsilon_{topology\ cuts} \cdot \varepsilon_{mass\ window\ cuts} \tag{8.2}$$

where $\sigma_{95\,\%\,limit}$ is the 95 % confidence level (C.L.) limit of the technicolor production cross section, $N_{95\,\%\,limit}$ is the 95 % C.L. limit of the number of TC signal event on the background, and ε_{total} is the total efficiency of the TC signal detection.

We used a simple Monte Carlo to determine the $N_{95\,\%\,limit}$. This Monte Carlo first determines the number of background events and the number of signal events in a trial from Poisson distribution with means $N_{background}$ and N_{signal}, respectively. These means are varied within Gaussian distributions with widths given by their errors (truncated at zero). The confidence level for the limit is given by the fraction of kept trials which have a total number of events exceeding the observed number. The value for N_{signal} is scanned until the confidence level is 95%.

Table 8.1 shows N_{signal}, $N_{background}$, N_{data} with the production cross section, and 95 % C.L. upper limits on the number of signal events event and the production cross section upper limits for all mass combinations. In Figure 8.1, the 95 % C.L. limits on the production cross section and the theoretical production cross sections are plotted as a function of M(ρ_T). Eight plots are similar, but the technipion masses are changed from 80 GeV/c^2 to 115 GeV/c^2 in 5 GeV/c^2 step. From these plots, we can see the 95% C.L. excluded region in M(ρ_T) for each M(π_T) value. As a summary plot, in Figure 8.2, we show the 95 % C.L. excluded region as a filled area in the M(π_T) vs. M(ρ_T) space. The expected theoretical cross section $[\sigma(p\bar{p} \to \rho_T^{\pm} \to W+\pi_T^0) + \sigma(p\bar{p} \to \rho_T^0 \to W+\pi_T^{\pm})]$ is drawn as contours in the same plane.

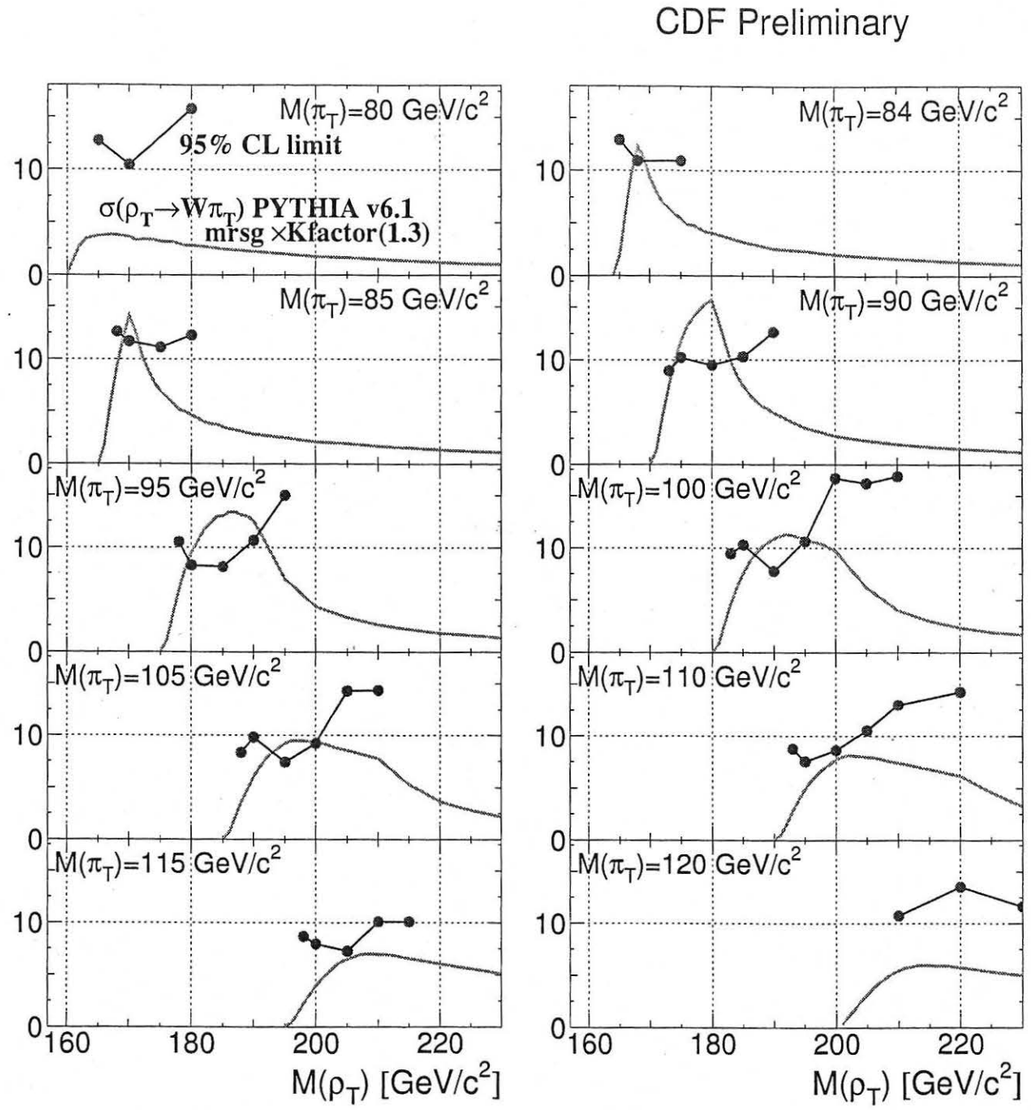

Figure 8.1: Solid circle show 95 % confidence level upper limits on the ρ_T production cross section as a function of M(ρ_T) for different M(π_T) masses. Solid curve is the theoretical production cross section times branching ratio of $\rho_T^{\pm} \to W+\pi_T^0$ and $\rho_T^0 \to W+\pi_T^{\pm}$. PYTHIA v 6.1, CTEQ4L pdflib, and a K-factor(1.3) are used to calculate the cross section .

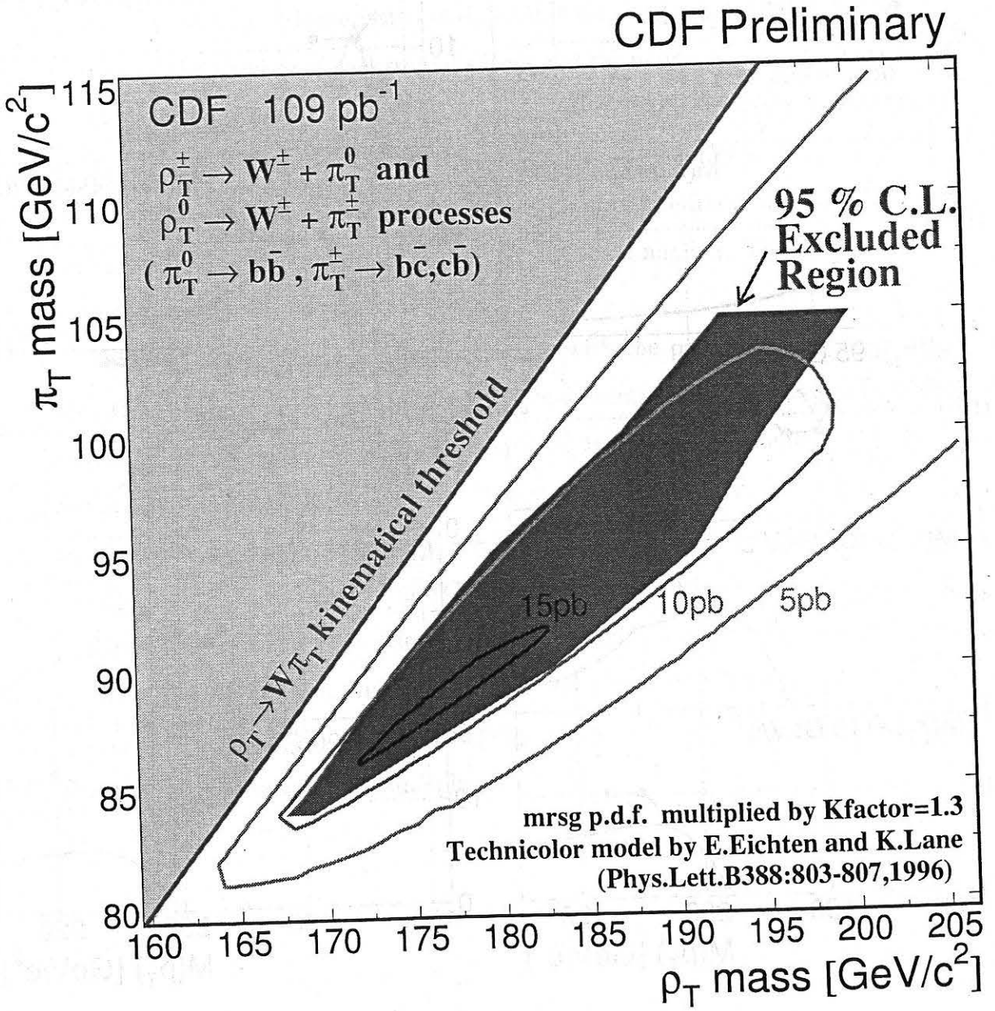

Figure 8.2: The 95 % C.L. excluded region in the M(π_T),M(ρ_T) plane. The theoreti cross section $[\sigma(p\bar{p} \to \rho_T^{\pm} \to W + \pi_T^0) + \sigma(p\bar{p} \to \rho_T^0 \to W + \pi_T^{\pm})]$ is drawn as a contc plot in the same plane.

Chapter 9

Summary

We have searched for technicolor particles, π_T and ρ_T, in $p\bar{p}$ collisions at $\sqrt{s} = 1.8$ TeV using an integrated luminosity of $109 \pm 7\,\mathrm{pb}^{-1}$ in the CDF data. We have looked for the $\rho_T^{\pm} \to W + \pi_T^0$ and the $\rho_T^0 \to W + \pi_T^{\pm}$ modes by analyzing the leptonic decayed W boson with b-tagged two jets final state. We have searched for a technipion mass resonance in the invariant mass distribution of b-tagged two-jet system and a technirho mass resonance in the invariant mass distribution of W and b-tagged two jets system. Technicolor theory expects that the sharp mass resonances of the technipion and the technirho appear on the background of broad mass spectrum expected from the Standard Model. Our search has been done for the forty-seven different mass combinations of the technipion and the technirho from the lowest mass combination, M(π_T)=80 GeV/c^2 and M(ρ_T)=165 GeV/c^2 , to the highest mass combination, M(π_T)=120 GeV/c^2 and M(ρ_T)=230 GeV/c^2 . These mass combinations cover the mass combination region whose cross section is expected to be sufficiently high to find the technipion and the technirho if they exist.

Any signature of our search modes has not been found at all; the CDF data under consideration is completely consistent with the predictions of the Standard Model. From the statistics of the data and the background, we set an upper limit of the production cross section for each mass combination of the technipion and the technirho with 95 % confidence level and set an excluded region in the mass plane of these technicolor particles as shown in Figure 8.2 .

Bibliography

[1] S. Weinberg, Phys. Rev. **D19** No.4, 1277 (1979).

[2] L. Susskind, Phys. Rev. **D20** No.10, 2619 (1979).

[3] For a recent review see S. F. King, Rep. Prog. Phys. **58**, 263 (1995).

[4] K. Lane and M. V. Ramana, Phys. Rev. **D44**, 2678 (1991).

[5] Estia Eichten, Kenneth Lane Phys. Lett. **B388**, (1996).

[6] K. Lane and E. Eichten Phys. Lett. **B222**, 274 (1989).
E. Eichten and K. Lane FERMILAB-CONF-96/297-T .

[7] Kenneth Lane hep-ph/9801385 .

[8] Estia Eichten, Kenneth Lane hep-ph/9607213 .

[9] T. Sjostrand, Comp. Phys. Comm. **82**, 74 (1994) (We use PYTHIA version 6.1)
'http://www.thep.lu.se/tf2/staff/torbjorn/Pythia.html' .

[10] F.Abe *et. al.* Phys. Rev. Lett. **76**, 17 (1996).

[11] R. Vilar, T.Handa, K.Maeshima, T.Rodrigo, and J.Valls, CDF internal nc
No.4543 .

[12] A.D. Martin *et. al.* hep-ph/9502336 .

[13] Vernon D. Barger, Roger J.N. Phillips, Collider Physics .

[14] Estia Eichten, Kenneth Lane, and John Womersley Phys. Lett. **B405**, 305 (1997).

[15] F.Abe *et. al.* Phys.Rev. **D45**, 1448 (1992).

[16] F.Abe *et. al.* Phys.Rev. **D47**, 4857 (1993).

[17] F.Abe *et al.* Nucl. Inst. Methods Phys. Res. Sect. **A271**, 387 (1998).

[18] U. Amaldi *et. al.* Phys. Lett. **B447** (1991).
P. Langacker *et. al.* Phys. Lett. **D44**, 817 (1991).

[19] D.Amidei *et. al.* Nucl. Inst. Methods **A269**, 51 (1988).

[20] G.Ascoli *et. al.* Nucl. Inst. Methods **A269**, 63 (1988).

[21] J.T. Carrol *et. al.* Nucl. Inst. Methods **A300**, 552 (1991).

[22] F.Abe *et. al.* Phys.Rev. **D52**, 5 (1991).

[23] F.Abe *et. al.* Phys. Rev. Lett. **64**, 142 (1990).
F.Abe *et. al.* Phys. Rev. **D43**, 664 (1991).

[24] F.Abe *et. al.* Phys. Rev. **D50**, 5 (1994).

[25] F.Abe *et. al.* Phys.Rev. **D45**, 7 (1992).

[26] F.Abe *et. al.* Phys. Rev. Lett. **72**, 3456 (1994).

[27] M.L.Mangano, Nucl. Phys. **B405**, 536 (1993) .

[28] Guillaume Unal *et.al.* CDf internal note No.3513 .

[29] Y. Cen *et.al.* CDF internal note No.2965 .

[30] F.Abe *et. al.* Phys. Rev. Lett. **74**, 14 (1995).

[31] T. Kikuchi *et.al.* CDF internal note No.4542 (1998).

[32] G. Marchesini *et. al.* Comput. Phys. Commun. **67**, 465 (1992).

[33] F.A. Berends *et. al.* Nucl. Phys. **B357**, 32 (1991).

[34] D. Gerdes, in Proceedings of the Morriond Conference FERMILAB-CONF-97-166-E (1997).

[35] Martin C. Smith *et. al.* Phys.Rev. **D54**, 11 (1996).

[36] F.Abe *et. al.* Phys. Rev. Lett. **79**, 20 (1997).

公表論文

(1) Search for Higgs Bosons Produced in Association with a Vector Boson in $p\bar{p}$ Collisions at $\sqrt{s}$ = 1.8 TeV

重心系エネルギー 1.8 TeV 陽子・反陽子衝突におけるヒッグス粒子探索

Physical Review Letters, Volume 81, Number 26, 5748-5753
平成10年12月28日出版(The American Physical Society)

(2) Measurement of the Top Quark Mass with the Collider Detector at Fermilab

フェルミ研究所 CDF 実験におけるトップクォーク質量の測定

Physical Review Letters, Volume 82, Number 2, 271-276
平成11年1月11日出版(The American Physical Society)